

SCIENTIFIC REPORTS



OPEN

New insights into the origin of remote PPG signals in visible light and infrared

Received: 15 January 2018

Accepted: 3 May 2018

Published online: 31 May 2018

Andreia V. Moço¹, Sander Stuifk¹ & Gerard de Haan^{1,2}

Remote photoplethysmography (PPG) is an optical measurement technique with established applications in vital signs monitoring. Recently, the consensual understanding of blood volume variations (BVs) as the origin of PPG signals was challenged, raising validity concerns about the remote SpO₂ methodology. Recognizing the imperative for new opto-physiological evidence, this investigation supports the volumetric hypothesis with living skin experiments and Monte Carlo simulations of remote PPG-amplitude in visible light (VIS) and infrared (IR). Multilayered models of the skin were developed to simulate the separate contributions from skin layers containing pulsatile arterioles to the PPG signal in the 450–1000 nm range. The simulated spectra were qualitatively compared with observations of the resting and compressed finger pad, and complemented with videocapillaroscopy. Our results indicate that remote PPG systems indeed probe arterial blood. Green wavelengths probe dermal arterioles while red-IR wavelengths also reach subcutaneous BVs. Owing to stable penetration depths, the red-IR diagnostic window promotes the invariance of SpO₂ measurements to skin non-homogeneities.

Photoplethysmography (PPG) is an optical measurement technique that has advanced technically, achieving ubiquity in current clinical settings¹ and the status of enabling technology for non-obtrusive innovations in pulse-rate and SpO₂ monitoring^{2–5}. Various sensing modalities are available for probing PPG signals. Its fundamental distinction is in whether signals are acquired in transmission or in reflection mode. Transmission-based acquisition requires the illuminating source and photosensor to face opposing sides of the tissue, whereas the latter has these elements on the same side. Transmission-mode PPG results from minute cardiac-related modulations of skin absorbance and is ubiquitous in most finger pulse oximeters (see Fig. 1a).

Camera-based systems can operate in transmission-mode⁶, but are better suited for remote reflectance measurements. Remote PPG allows that the pulse-rate is extracted, preferentially, at green wavelengths, though a quest for motion robustness deems necessary that multiple wavelength bands (color-channels) are combined⁷. The red-IR diagnostic window has also been shown suitable for PPG-based measurements, including SpO₂⁸.

PPG systems continue to mature by exploring of the PPG signal's frequency diversity. Multispectral PPG data, in VIS–IR, may find clinical value in skin health assessments^{9,10}. While multispectral cameras remain prohibitively expensive and computationally heavy, multispectral PPG can be acquired by coupling a spectrometer with an optical fiber probe (OFP; see Fig. 1c). Since there is contact of the probe with the skin, we refer to this setting as reflection-mode acquisition.

Importance of investigating the origin of the PPG signal

It may come as a surprise that the PPG-based techniques and applications have developed more than the opto-physiological knowledge pertaining to the origin of the signal, which remains vaguely referred to as arterial blood volume variations (BVs) occurring at every cardiac heart beating within the microvascular bed of tissue. Still, the understanding of PPG as BVs, which we shall refer to as the volumetric model, has been able to support the working principle of current PPG-based applications. In particular, the volumetric model provides a rationale for using PPG as a surrogate of the arterial blood oxygenation curve. The enabling principle is the dependency between normalized PPG-amplitude ratios at red-IR wavelengths, and the relative proportion between oxygenated and non-oxygenated haemoglobin absorption^{3,11}.

¹Department of Electrical Engineering, Eindhoven University of Technology, 5612AZ, Eindhoven, The Netherlands.

²Philips Innovation Group, Philips Research, High Tech Campus 36, 5656AE, Eindhoven, The Netherlands. Correspondence and requests for materials should be addressed to A.V.M. (email: a.moco@tue.nl)

SCIENTIFIC REPORTS



OPEN

对可见光和红外线中远程PPG信号起源的新见解

收到日期：2018年1月15日

接受日期：2018年5月3日

发布时间：xx xx xxxx May 2018

Andreia V. Young, Sander Stuijk 和 Gerard de Haan

远程光电容积描记术（PPG）是一种光学测量技术，在生命体征监测中具有既定的应用。最近，血容量变化（BVV）作为PPG信号来源的共识受到挑战，引起了对远程SpO方法的有效性担忧。认识到新的光生理证据的必要性，这项调查支持活皮肤实验和Monte Carlo模拟可见光（VIS）和红外（IR）中的远程PPG幅度的体积假设。开发了皮肤的多层模型，以模拟包含脉动小动脉的皮肤层对450-1000 nm范围内的PPG信号的单独贡献。模拟光谱进行了定性比较与休息和压缩的手指垫的观察，并补充与videocapillaroscopy。我们的研究结果表明，远程PPG系统确实探测动脉血。绿色波长探测真皮小动脉，而红色-IR波长也到达皮下BVV。由于稳定的穿透深度，

诊断窗口促进了SpO测量对皮肤非均匀性的不变性。

光电容积描记术（PPG）是一种光学测量技术，在技术上取得了进步，在当前临床环境中普遍存在，并在脉搏率和SpO监测中实现了非侵入性创新的技术状态。各种感测模态可用于探测PPG信号。其基本区别在于信号是以透射模式还是以反射模式获取的。基于透射的采集要求照明源和光传感器面向组织的相对侧，而后者在同一侧具有这些元件。传输模式PPG由皮肤吸收的心脏相关微小调制产生，在大多数手指脉搏血氧仪中普遍存在（见图1a）。

基于相机的系统可以在传输模式下工作，但更适合远程反射测量。远程PPG允许优先地在绿色波长处提取脉搏率，尽管对运动鲁棒性的追求认为组合多个波长带（颜色通道）是必要的。红色-IR诊断窗口也被证明适用于基于PPG的测量，包括SpO。

PPG系统通过探索PPG信号的频率多样性而不断成熟。VIS-IR中的多光谱PPG数据可能在皮肤健康评估中具有临床价值。虽然多光谱相机仍然非常昂贵且计算量很大，但可以通过将光谱仪与光纤探头（OFP;参见图1c）耦合来获取多光谱PPG。由于探头与皮肤接触，我们将此设置称为反射模式采集。

研究PPG信号来源的重要性

令人惊讶的是，基于PPG的技术和应用已经发展了超过与信号起源有关的光学生理学知识，信号起源仍然模糊地称为了在组织的微血管床内的每次心脏跳动时发生的动脉血容量变化（BVV）。尽管如此，将PPG理解为BVV（我们将其称为体积模型）已经能够支持当前基于PPG的应用的工作原理。特别地，体积模型提供了使用PPG作为动脉血氧合曲线的替代的基本原理。使能原理是在红色-IR波长处的归一化PPG幅度比与氧合血红蛋白吸收和非氧合血红蛋白吸收之间的相对比例之间的依赖性。

¹荷兰埃因霍温，5612 AZ，埃因霍温理工大学电气工程系。

² Philips Innovation Group, Philips Research , High Tech Campus 36, 5656 AE, 埃因霍温, 荷兰。有关材料的信函和请求应提交给A.V.M.。（电子邮件：a.tue.nl）

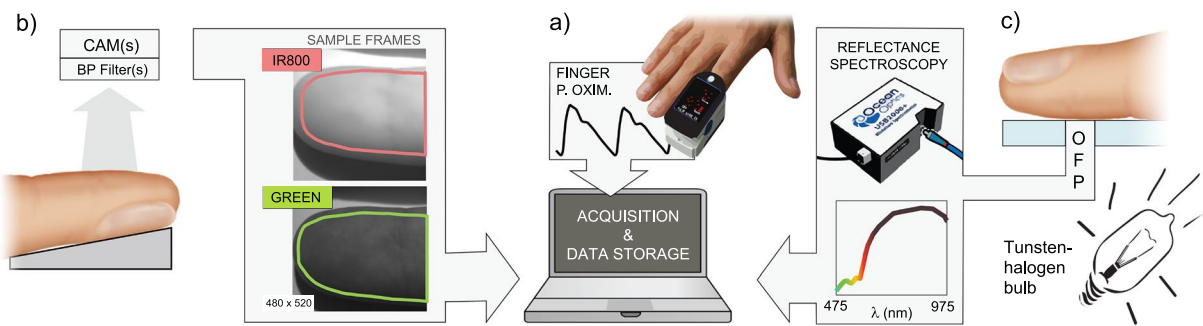


Figure 1. PPG signals can be acquired (a) in transmission-mode, e.g., by finger pulse oximetry, (b) remotely, or (c) in reflectance-mode, e.g., by using a spectrometer (OFP, optical fiber probe). The figure was created by A. Moço.

The volumetric model is consensual but not unique¹. For example, flow variations have been suggested as a mechanism for inducing light reflectance variations^{12,13}. Naslund *et al.*¹² observed reflection-mode PPG signals by using IR wavelengths in the patellar bone, a site where vessel wall distensions are not theoretically possible. It remains uncertain whether this observation is spurious contamination by surrounding pulsatile tissue. More reliable optical insights on PPG generation may be obtained by investigating blood flow in phantoms. Lindberg¹³ showed that blood reflection changes if a liquid solution containing red blood cells (RBCs) flows in a rigid tube. When the flow velocity and concentration of the solution are such that periodic RBC aggregation takes place (i.e., haematocrit levels above 38%), the blood reflection reflects the changes in the orientation and deformability of the RBCs¹³. On a similar setup, Shvartsman¹⁴ simulated pulsatile blood flow and confirmed that PPG-like signals are associated with geometric changes in RBC aggregation¹⁴.

Recently, Kamshilin *et al.*¹⁵ reported conflicting observations with the volumetric model¹⁶. One of such observations were counter-phase PPG signals in the vicinity of the radial or brachial artery, which are simply motion artifacts^{17,18}. A more interesting argument raised against the volumetric model was the apparent paradox that the PPG-amplitude peaks in green, although it would not, theoretically, even reach pulsating arterioles. Gently compressing the skin against a glass plate increases the green PPG-amplitude further, which, again, appears to find no explanation in the volumetric model.

Consequently, a new theory was proposed, drawing attention to elastic deformations of the dermis as dominant mechanism of PPG formation. The increasing transmural pressure of the arteries during systole would compress the dermal connective tissue and increase the overall capillary density. These deformations would explain the observed gains under compression. However, if arterial BVVs are not the origin of PPG, concerns emerge when it comes to the validity of PPG-based SpO_2 measurements. In fact, if the total dermal tissue is periodically compressed, then PPG-based SpO_2 readings would not be possible as these would be severely contaminated by venous pulsations.

Supporting and broadening the application scopes of PPG requires that the depth-origin of the signal is confirmed and its origin explained. Thus, it is imperative that the volumetric model is revised in light of the recent experiments devised by Kamshilin¹⁵. If it could be shown that even visible light penetrates deep enough to interact with arterioles, then the confidence on the volumetric model would be enforced. In this paper we tackle this topic under the hypothesis that the volumetric model is true and take a combined numerical and experimental approach. The skin was modeled as multilayered media with optical properties that translate its anatomophysiology¹⁹. Then the Monte Carlo method was applied to simulate the PPG-amplitude spectra; its verification on living skin validated, indirectly, the volumetric model assumption.

Modeling the skin's microvasculature

The inhomogeneity of the microvasculature was accounted by representing the non-glabrous skin structure as a medium split into six stacked horizontal layers (see Fig. 2a). The first layer corresponds to the epidermis (EPI), which is bloodless²⁰ and consists of mostly dead or dehydrated cells and no melanosomes. The thickness of the epidermis is highly skin-site dependent, but 0.8 mm is reasonable for the finger pad. The dermis was subdivided into four layers with different blood concentrations, which are as follows²¹: capillary loops (CL; 150–200 μm thick); upper plexus (UP; 80 μm thick), reticular dermis (RD; 1400–3000 μm thick); and deep plexus (DP; 80–700 μm thick). The arterial compartment in the plexuses and RD represent arterioles supplying the entire tissue volume and venules collecting the returning venous blood. The deepest layer of the model is the subcutis (SC; or hypodermis), which accounts for fat, connective tissue and pulsating arterioles or arteries.

Our hypothesis that BVVs are located at the dermal plexuses, RD and SC is partly in agreement with prior work of Reuss²², where it is assumed that only the plexuses contribute to PPG formation, but not with Huelsbusch²³, who modeled the PPG's origin at the capillary loops only. However, Huelsbusch's PPG-amplitude spectrum largely underestimated the relative amplitude of signals in red-IR wavelengths, suggesting the incorrectness of this parameter setting.

We implemented models that mimic the opto-physiological contribution of the skin layers to the total reflectance-mode PPG spectra, separately, for normal and compressed skin (see Fig. 2a,b, respectively). Recognizing each of these contributions as the layer's "signatures", the overall remote PPG signal is in fact a

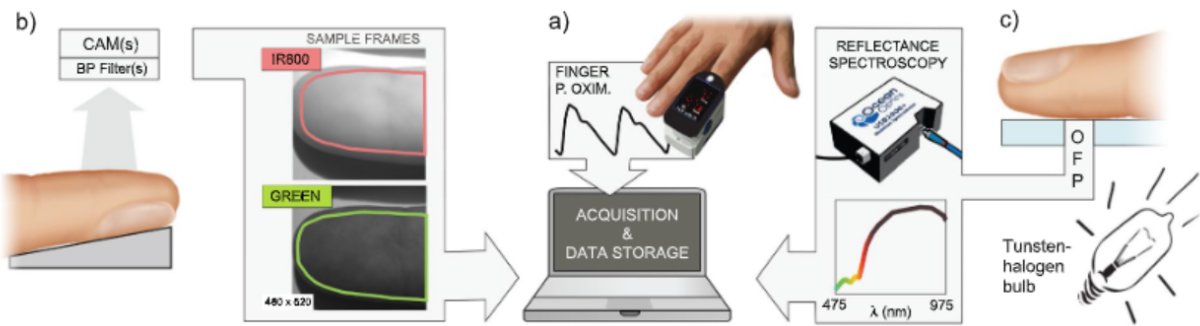


图1. PPG信号可以(a)在传输模式下采集,例如,通过手指脉搏血氧仪,(b)远程地,或(c)以反射模式,例如,通过使用光谱仪(OFP,光纤探针)。这个图形是由A.莫索

体积模型是协商一致的,但不是唯一的。例如,已经提出流动变化作为用于引起光反射率变化的机制。Naslund等人通过使用髌骨中的IR波长观察到反射模式PPG信号,髌骨是血管壁扩张在理论上不可能的部位。目前还不确定这一观察结果是否是周围脉动组织的虚假污染。通过研究体模中的血流,可以获得关于PPG生成的更可靠的光学见解。林德伯格表明,如果含有红细胞(RBC)的液体溶液在刚性管中流动,血液反射会发生变化。当溶液的流速和浓度使得发生周期性RBC聚集时(即,当红细胞压积水平高于38%时),血液反射反映了RBC的取向和变形性的变化。在一个类似的装置上,Shvartman模拟了脉动血流,并证实了PPG样信号与RBC聚集的几何变化有关。

最近,Kamshilin等人报道了与体积模型相矛盾的观测结果。这些观察结果之一是桡动脉或肱动脉附近的反相PPG信号,其仅仅是运动伪影。针对容积模型提出的一个更有趣的论点是明显的悖论,即PPG幅度峰值为绿色,尽管理论上它甚至不会到达脉动的小动脉。轻轻地将皮肤压在玻璃板上进一步增加了绿色PPG幅度,这在体积模型中似乎也找不到解释。

因此,提出了一种新的理论,提请注意作为PPG形成的主要机制的真皮的弹性变形。收缩期动脉跨壁压的增加会压迫真皮结缔组织,增加毛细血管的整体密度。这些变形可以解释在压缩下观察到的增益。然而,如果动脉BVV不是PPG的来源,则在涉及基于PPG的SpO测量的有效性时会出现问题。事实上,如果整个皮肤组织被周期性地压缩,则基于PPG的SpO读数将是不可能的,因为这些将被静脉搏动严重污染。

支持和拓宽PPG的应用范围,需要确定信号的深度来源并解释其来源。因此,必须根据Kamshilin最近设计的实验对体积模型进行修订。如果能够证明即使可见光也能穿透足够深以与小动脉相互作用,则将加强对体积模型的置信度。在本文中,我们解决这个问题的假设下,体积模型是真实的,并采取相结合的数值和实验方法。皮肤被建模为多层介质的光学特性,翻译其解剖生理学。然后应用Monte Carlo方法模拟了PPG幅度谱,并在活体皮肤上进行了验证,间接验证了体积模型假设。

模拟皮肤的微血管系统

通过将非光滑皮肤结构表示为分成六个堆叠水平层的介质来解释微脉管系统的不均匀性(参见图2a)。第一层对应于表皮(EPI),它是无血的,主要由死亡或脱水的细胞组成,没有黑素体。表皮的厚度高度依赖于皮肤部位,但0.8 mm对于指垫是合理的。真皮分为四层,具有不同的血液浓度,如下:毛细血管袢(CL; 150-200 μm厚);上丛(UP; 80 μm厚);网状真皮(RD; 1400-3000 μm厚);和深丛(DP; 80-700 μm厚)。丛和RD中的动脉隔室代表供应整个组织体积的小动脉和收集返回的静脉血液的小静脉。模型的最深层是皮下组织(SC;或皮下组织),其负责脂肪、结缔组织和脉动小动脉或动脉。

我们假设BVV位于真皮丛、RD和SC,这与Reuss先前的工作部分一致,其中假设只有丛有助于PPG形成,但Huelsbusch不同意,Huelsbusch仅在毛细血管袢处模拟PPG的起源。然而,Huelsbusch的PPG幅度谱在很大程度上低估了红红外波长信号的相对幅度,这表明该参数设置不正确。

我们分别针对正常皮肤和压缩皮肤实现了模拟皮肤层对总反射模式PPG光谱的光生理贡献的模型(分别参见图2a、b)。将这些贡献中的每一个识别为层的“签名”,总体远程PPG信号实际上是一个

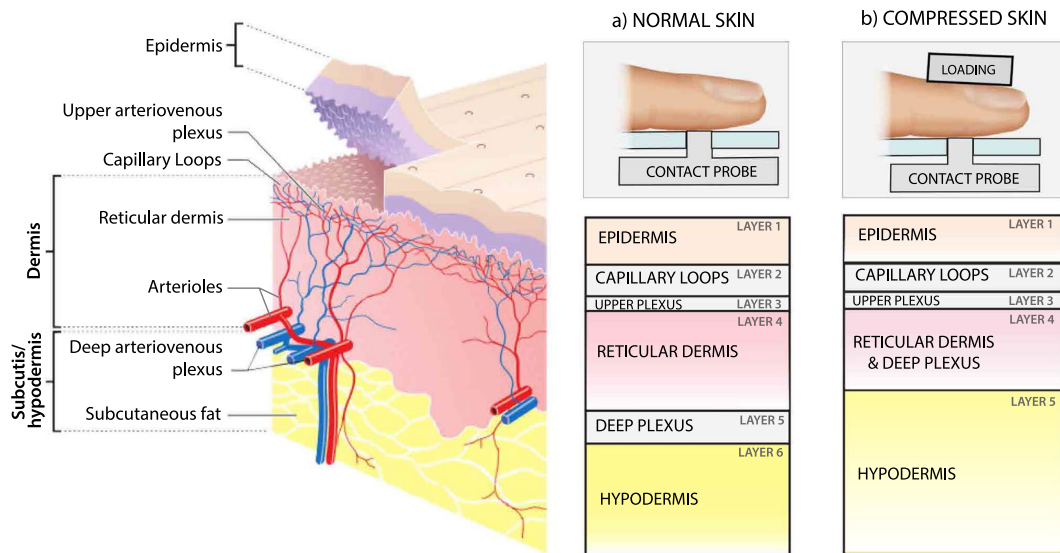


Figure 2. Skin represented as multiple stacked horizontal layers for (a) normal conditions and (b) for compression. The normal skin is modeled as epidermis (EPI); capillary loops (CL); upper plexus (UP); reticular dermis (RD); deep plexus (DP); and subcutis (SC). The compressed skin has reduced blood content and allows the light to penetrate deeper into the skin. On a contact-based setup, compression is achieved by loading the finger pad against the probe. The figure was built by A. Moço upon the skin layers of Madher088, via Wikimedia Commons (en.wikipedia.org/wiki/File:Skin_layers.png, CC BY-SA 3.0).

mixture of the dermal and subdermal signatures. A useful as proof-of-concept for the volumetric model hypothesis is to isolate and demonstrate these signatures. However, the mixing weights are unknown, which is also why the compression intervention is valuable in this study.

Strong compression, yet below the systolic pressure level, is a simple intervention to block the dermal BVVs and blanch the skin, hence isolating the signatures from deeper pulsating structures in the PPG spectra of the compressed skin and allowing the incident light to reach deeper layers. Under full occlusion of the upper dermis, only the DP and SC remain pulsatile, and the removal of venous blood leads to its contributions being much stronger than in normal conditions. When sustained, metabolites accumulate and arterial vasodilation is also triggered^{24,25}. To translate these effects in simulations, the compressed skin is modeled by the similar layers as the normal/reference skin (1-EPI; 2-CL; 3-UP; 4-RD & DP and 5-SC & digital artery). However, reductions are made to blood and water concentrations, layer's thickness, whereas the relative strength BVVs from deeper layers is boosted. We remark that both skin models translate biological tissue heterogeneity in the depth dimension only, which is suitable for pointwise diffuse reflectance spectroscopy (DRS) measurements.

The skin layers signatures were generated by perturbing the diffuse reflectance of the skin's model. Specifically, a systolic event corresponds to an influx of arterial blood to the skin tissue and was implemented as minute increments in the absorption coefficient of the dermal and subdermal layers with respect to diastolic-state reflectance of the model. Whenever possible, parameters conform to the literature. Otherwise, these were calibrated based on our own camera-based/remote measurements.

The next section is devoted to the results and discussion of our measurements and simulations. A methods section follows with a detailed description of the videocapillaroscopy protocol and implementation details of the Monte Carlo simulations.

Results and Discussions

Experimental Setups. This study comprises two experimental parts. Part 1 includes a comparison of PPG signals acquired with cameras in the green wavelength range and in IR, as well as insights from videocapillaroscopy and DRS. This part offers helpful observations for calibrating skin tissue simulations. For convenience, skin measurements were performed at the human finger (pad and nail fold). The skin of the finger pad is glabrous (non-hairy) and offers the advantages of strong PPG signals, negligible melanin content and ease of stabilization. The nail fold also allows acquisition of strong PPG signals and has the peculiarity of having the capillary loops oriented in parallel to the skin surface, which enables their observation by regular reflectance microscopy. Part 2 compares simulations and measurements of the PPG spectra in normal and compressed skin.

Experimental Part 1: Multimodal remote PPG observations. *Camera-based PPG in VIS versus IR.* Figure 3 illustrates our framework for comparing PPG signals in VIS-green and IR with data acquired on a subject from this study (SpO_2 level, 95–98%; seated position) for a finger pad measurement performed 20–30 cm below the heart level (imaging area, about 100 mm^2). The pad was measured with a monochrome camera (sampling rate, 30 Hz) under stable lighting conditions (incandescent bulb; 9 V, DC). Two consecutive measurements were performed using optical bandpass filters that isolate the green wavelength range (center frequency/unilateral

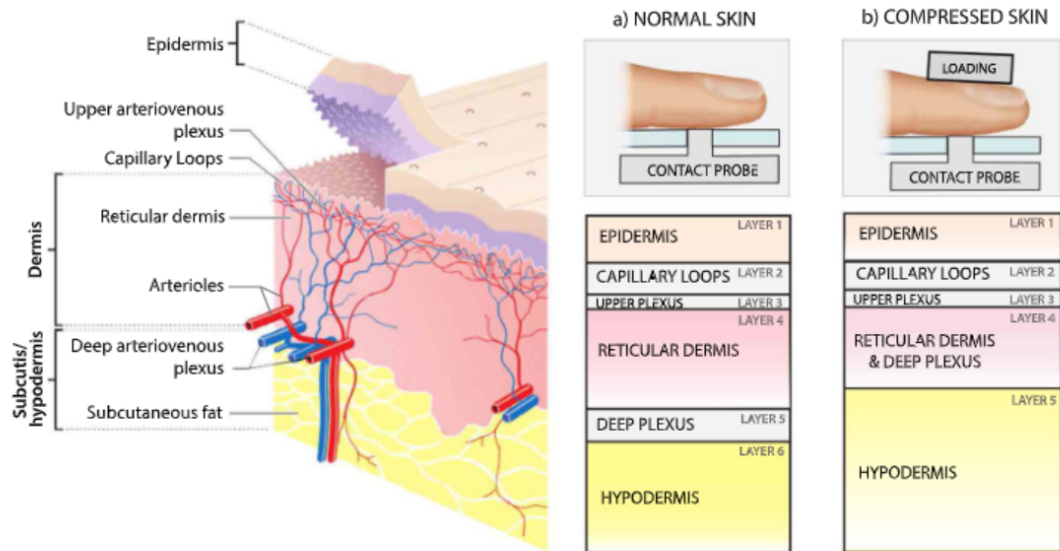


图2.对于(a)正常条件和(b)压缩条件,皮肤表示为多个堆叠的水平层。正常皮肤被建模为表皮(EPI);毛细血管网(CL);上丛(UP);网状真皮(RD);深丛(DP);和皮下组织(SC)。压缩的皮肤减少了血液含量,并允许光线更深地穿透皮肤。在基于接触的设置中,通过将指垫加载到探针上来实现压缩。这个数字是由A。Madhero 88皮肤层上的Moço,通过维基共享资源(en.wikipedia.org/wiki/File:Skin_layers.png, CC BY-SA 3.0)。

混合了真皮和皮下的特征体积模型假设的一个有用的概念验证是隔离和证明这些签名。然而,混合权重是未知的,这也是为什么压缩干预在本研究中是有价值的。

强压缩,但低于收缩压水平,是一种简单的干预,以阻止真皮BVV和漂白皮肤,因此隔离的签名从更深的脉动结构在PPG光谱的压缩皮肤,并允许入射光到达更深层。在真皮上层完全闭塞的情况下,只有DP和SC保持搏动,并且静脉血的去除导致其贡献比正常情况下强得多。当持续时,代谢物积聚并且还触发动脉血管舒张。为了在模拟中转换这些效果,压缩皮肤由与正常/参考皮肤类似的层(1-EPI; 2-CL; 3-UP; 4-RD & DP和5-SC &指动脉)建模。然而,血液和水的浓度,层的厚度,而从更深的层的相对强度BVV的提高。我们注意到,这两种皮肤模型只在深度维度上转换生物组织的异质性,这适合于逐点漫反射光谱(DRS)测量。

皮肤层签名是通过扰动皮肤模型的漫反射来生成的。具体而言,心脏收缩事件对应于动脉血流入皮肤组织,并且被实施为真皮和皮下层的吸收系数相对于模型的吸收状态反射率的微小增量。只要有可能,参数应符合文献。否则,这些都是根据我们自己的基于相机/远程测量校准的。

下一节将专门讨论我们的测量和模拟的结果和讨论。方法部分随后详细描述了视频毛细血管镜检查方案和蒙特卡罗模拟的实施细节。

结果和讨论

实验设置。本研究包括两个实验部分。第1部分包括在绿色波长范围和IR中使用摄像机采集的PPG信号的比较,以及来自视频毛细血管镜检查和DRS的见解。这部分为校准皮肤组织模拟提供了有用的观察结果。为方便起见,在人手指(指腹和甲襞)处进行皮肤测量。指垫的皮肤是无毛的(无毛),并且提供了强PPG信号、可忽略的黑色素含量和易于稳定的优点。甲襞还允许采集强PPG信号,并且具有使毛细血管环平行于皮肤表面取向的特性,这使得能够通过常规反射显微镜观察它们。第2部分比较了正常和压缩皮肤中PPG谱的模拟和测量。

实验部分1: 多模态远程PPG观察。

维斯中基于摄像头的PPG与IR。图3显示了我们的框架,用于将VIS-绿色和IR中的PPG信号与从本研究(SpO水平, 95-98%;坐姿)的受试者上采集的数据进行比较,用于在心脏水平以下20-30 cm(成像区域,约100 mm)进行指垫测量。在稳定的照明条件下(白炽灯泡;9V, DC)下用单色照相机(采样率, 30 Hz)测量垫。使用隔离绿色波长范围(中心频率/单边)的光学带通滤波器进行两次连续测量

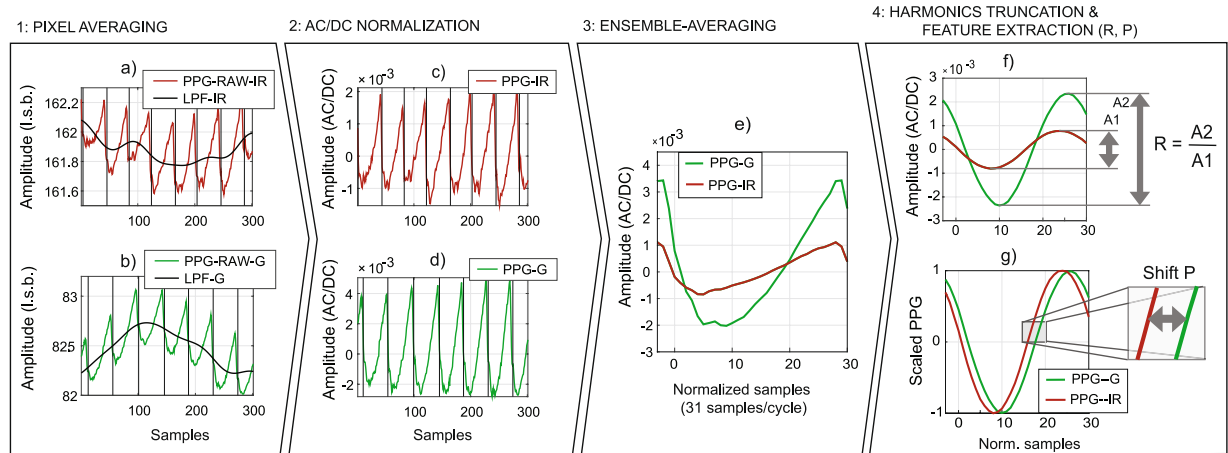


Figure 3. Processing pipeline: (1, 2) Remote-PPG signals acquired at the finger pad are low-pass-filtered and AC/DC-normalized; (3, 4) The AC/DC streams are ensemble-averaged (EA) (template size, 31 samples per cardiac cycle), including (e) multiple of the pulse-rate frequency and (f,g) the fundamental only.

bandwidth, 559/34 nm) and in IR (800/12 nm). Specifically, Fig. 3a,b show the average skin pixel intensity in consecutive samples for the green and IR recordings; i.e., “raw” PPG signals are the absolute diffuse reflectance of the skin over time. Similarly, Fig. 3c,d illustrate the normalized signals, resulting in periodic and zero-mean temporal series whose amplitude is typically upper bounded by 0.1. Consistent with the literature², we denote this format as “AC/DC” (abbreviation, “alternate current” over “direct current”). AC/DC normalization is performed by dividing the “raw PPG” (units, least significant bits; I.s.b.) by its low-pass filtered component (LPF).

After pixel averaging and normalization, two periodic and light-invariant PPG streams are obtained. These are polluted by sensor noise but ensemble-averaging (EA) cardiac cycles eliminates noise while retaining signal information (see Fig. 3e). Note that the amplitude difference between green and IR signals is consistent with the wavelength dependence of PPG and with the expectation that green and IR interact with the vasculature at different depths⁹.

Waveform dissimilarity is further evidenced when the EA waveforms are truncated to the fundamental of the pulse-rate frequency and scaled to unity (see Fig. 3f,g). An obvious feature for quantifying dissimilarity between two waveforms is the relative amplitude w.r.t. a reference wavelength. For example, when the reference is set at 800 nm, a ratio-of-ratios, R , can be computed as the standard deviation of the normalized green over IR (center wavelength, 800 nm) waveforms. For the pair of recordings depicted in Fig. 3, we measured an R of 2.9, but inter-individual differences can be large. On a small sample size ($N=4$), R was estimated to be 1.8 ± 0.8 . Subsequently, this range will be considered for calibrating the remote PPG spectra. Another useful feature for quantifying dissimilarity is the phase shift, P , which we illustrate at the fundamental of the signals. A non-zero P between wavelengths supports that the microvasculature is probed at different depths. In Fig. 3g, P was measured as 20 degrees, but test-retest experiments in other subjects suggest that the range of P is broad, ranging up to 30 degrees.

Videocapillaroscopy. Observing the capillary loops at the finger nail fold during PPG signal acquisition is insightful to investigate a possible contribution of capillaries to PPG. Owing to the low epidermal thickness at the nail fold, the capillary loops and arterioles are found as close to the surface as 0.28–0.43 mm and >0.43 mm, respectively²⁶, and can be reached using green light. Figure 4a shows our videocapillaroscopic setup and Fig. 4b a stable PPG segment, overlapped and its peaks and valleys in one subject.

When the frames corresponding to these critical instants are registered and averaged, separately for systole and diastole, the corresponding super-resolved images of the capillary loops are obtained (see Fig. 4(c,d)). The peak-to-peak (p2p) amplitude of the signal remains fairly stable during the selected segment and no differences were apparent in the density of visible capillaries. An useful approach to continue exploring data is to perform the normalized difference between the systolic and diastolic frames. The outcome is a PPG-amplitude image (PPGI, amplitude expressed as AC/DC-p2p; see Fig. 4e) which indicates that the PPG-amplitude is strongest where the blood concentration is highest (identified as darker regions in Fig. 4d). This interpretation is not confounded by the local density of capillary loops, which is fairly even across the imaged area. PPGI further shows that the gradient of the PPG strength varies smoothly across the skin surface and does not reflect the activity of isolated or clustered loops. This supports the hypothesis that the PPG in green is modulated by upper dermal arterioles.

Spectroscopic measurements of PPG on normal and compressed skin. This section shows our diffuse reflectance (DR) and reflectance-PPG spectra. 16 subjects were measured at normal conditions and under compression. One subject was excluded because the PPG signal in normal conditions was hidden by sensor noise. Figure 5a contrasts average DR spectra from the remaining 15 subjects of our dataset. The difference between these plots, ΔDR , is a wavelength-dependent function with relative peaks close to haemoglobin absorption (542 nm, 582 nm; see Fig. 5b).

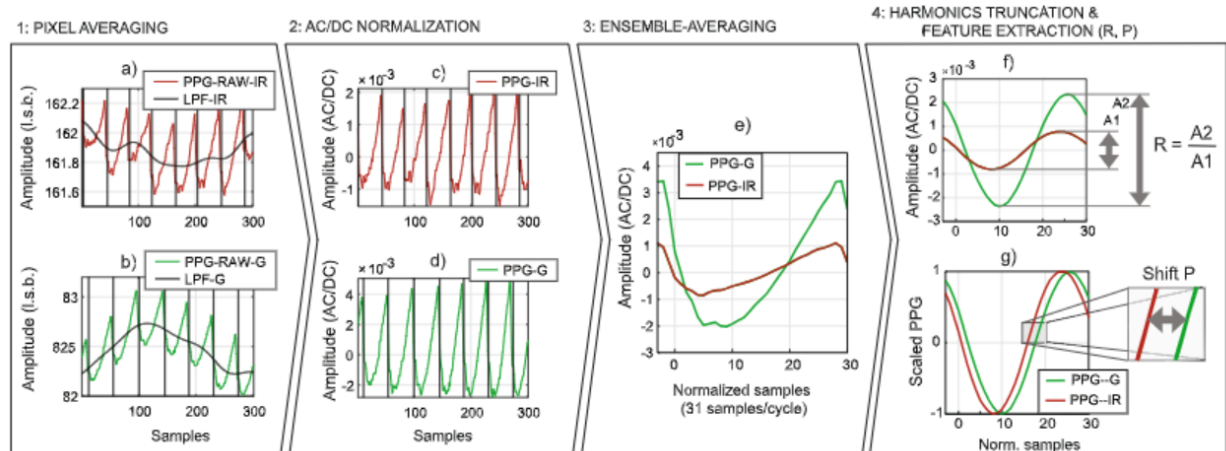


图3.处理管道：(1, 2) 对在指垫处采集的远程PPG信号进行低通滤波和AC/ DC归一化；(3, 4) 对AC/ DC流进行整体平均 (EA) (模板大小，每个心动周期31个样本)，包括 (e) 脉率频率的倍数和 (f, g) 仅基波。

带宽， $559/34\text{ nm}$ ）和IR（ $800/12\text{ nm}$ ）。具体地，图3a、B示出了绿色和IR记录的连续样本中的平均皮肤像素强度；即，“原始”PPG信号是皮肤随时间的绝对漫反射率。类似地，图3c、d示出了归一化信号，导致周期性和零均值时间序列，其幅度通常上限为0.1。与文献一致，我们将这种格式表示为“AC/ DC”（缩写，“交流电”超过“直流电”）。通过将“原始PPG”（单位，最低有效位；l.s.b.）低通滤波器（LPF）。

在像素平均和归一化之后，获得两个周期性和光不变的PPG流。这些被传感器噪声污染，但是整体平均 (EA) 心动周期消除了噪声，同时保留了信号信息（参见图3e）。注意，绿色和IR信号之间的幅度差与PPG的波长依赖性一致，并且与绿色和IR在不同深度处与脉管系统相互作用的预期一致。

当EA波形被截断到脉搏率频率的基波并缩放到单位时，波形的不相似性进一步得到证明（见图3f, g）。用于量化两个波形之间的不相似性的明显特征是相对幅度w.r.t.参考波长。例如，当参考被设置在 800 nm 时，比率的比率R可以被计算为归一化的绿色对IR（中心波长， 800 nm ）波形的标准偏差。对于图3所示的一对记录，我们测量的R为2.9，但个体间差异可能很大。在小样本量 ($N = 4$) 下，R估计为 1.8 ± 0.8 。随后，该范围将被考虑用于校准远程PPG光谱。量化相异性的另一个有用的特征是相移P，我们在信号的基础上说明。波长之间的非零P支持在不同深度探测微脉管系统。图3g, P被测量为20度，但在其他科目的重测实验表明，P的范围很广，范围高达30度。

视频毛细血管镜检查。在PPG信号采集期间观察指甲褶皱处的毛细血管环路对于研究毛细血管对PPG的可能贡献是有见地的。由于甲襞处的表皮厚度较低，毛细血管祥和小动脉分别接近表面 $0.28\text{--}0.43\text{ mm}$ 和 $>0.43\text{ mm}$ ，并且可以使用绿色光到达。图4a显示了我们的视频毛细血管镜设置，图4 b显示了一个受试者中重叠的稳定PPG段及其峰和谷。

当对应于这些关键时刻的帧分别针对收缩期和舒张期被配准和平均时，获得毛细血管祥的对应超分辨率图像（参见图4 (c, d)）。信号的峰-峰 (p2p) 幅度在选定的段期间保持相当稳定，可见毛细血管的密度没有明显差异。继续探索数据的有用方法是执行收缩帧和舒张帧之间的归一化差异。结果是PPG振幅图像 (PPGI，振幅表示为AC/ DC-p2p；参见图4 e)，其指示在血液浓度最高的地方（在图4d中标识为较暗区域）PPG振幅最强。这种解释不会被毛细血管圈的局部密度所混淆，毛细血管圈的局部密度在整个成像区域相当均匀。PPGI进一步表明，PPG强度的梯度在皮肤表面上平滑变化，并且不反映孤立或聚集的环的活动。这支持了绿色的PPG由上真皮小动脉调节的假设。

正常和受压皮肤上PPG的光谱测量。本节显示了我们的漫反射 (DR) 和反射PPG光谱。16名受试者在正常条件下和压缩下进行了测量。1例受试者被排除，因为正常条件下的PPG信号被探头噪声隐藏。图5a对比了来自我们数据集的其余15个受试者的平均DR光谱。这些曲线之间的差异 ΔDR 是波长依赖性函数，其相对峰接近血红蛋白吸收 ($542\text{ nm}, 582\text{ nm}$ ；见图5 b)。

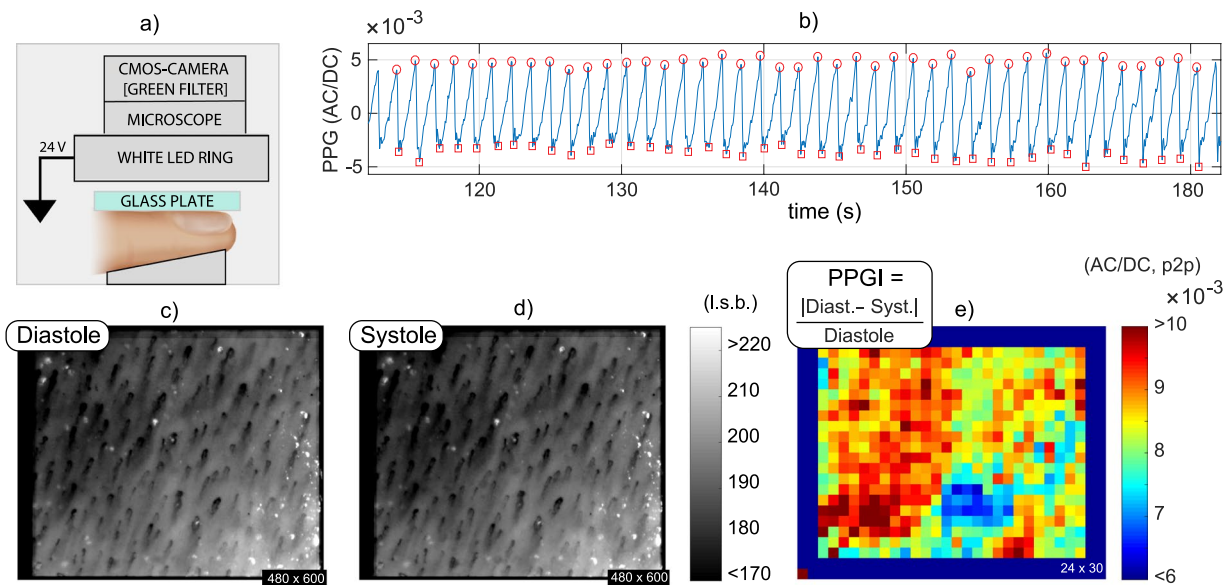


Figure 4. Videocapillaroscopic examination of the finger nail fold using green wavelengths: (a) Setup schematics; (b) Average PPG signal, with indication for systolic maxima (circles) and minima (squares); and super-resolved images of the upper dermis at the (c) peak instants and (d) valleys, respectively (imaging area, about 1.6×2 mm; amplification, $\times 60$). The downsized and normalized differential image between (c,d) is a PPGI-image (e) which suggests no relation between capillary density and PPG-signal strength. The figure was created by A. Moço.

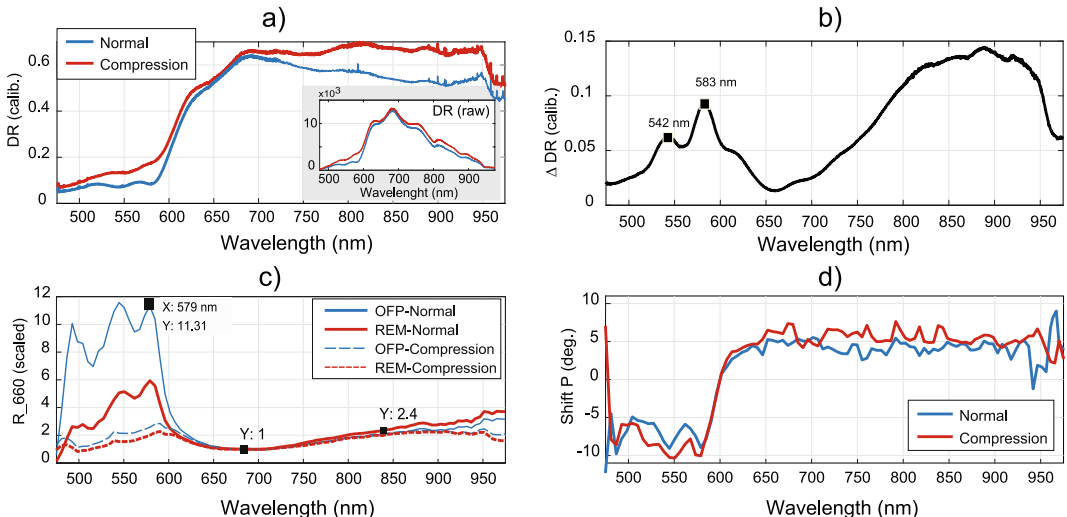


Figure 5. (a) DR profiles measured before and under skin compression; (b) the DR difference evidences the oxyhemoglobin absorption peaks. The cancellation of PPG at the VIS (<580 nm) range by compression is seen at the (c) scaled PPG-amplitude measurements (R_{660} ; OFP, optical fiber probe; REM, remote PPG). The (d) PPG-phase spectra shift at about 600 nm, which indicates shape dissimilarity between VIS and IR.

Figure 5c shows the medians of the PPG spectra obtained with the photometer-OFP system at normal and compressed skin ($N = 15$). Also included are the corresponding remote spectra estimated by using a transfer function (TF), which accounts for the skin properties and probe specifications (see the methods section for details). To ease comparisons, the PPG-amplitude spectra are scaled by its relative minimum at 660 nm and two variables were defined: the amplitude ratio of green over red (GoR, with green and red ranges defined at 520–577 nm and 660–700 nm, respectively), and the ratio of IR (range, 800–840 nm) over red (IRoR). In our dataset, paired-sample t-tests indicated that compression significantly reduces the average GoR by a factor of 4 (means \pm standard deviations; reference, 927 ± 319 ; compression, 2.32 ± 1.24 ; 1 rejected outlier; $p < 0.001$), whereas IRoR is not significantly affected (reference, 1.90 ± 0.16 ; compression, 1.95 ± 0.14 ; $p = 0.43$). This supports the multilayered BVVs hypothesis by evidencing that selectively blocking dermal layers affects the shallow PPG-green wavelengths. Note that the invariance of IRoR to compression holds for remote acquisition because the probe geometry is irrelevant

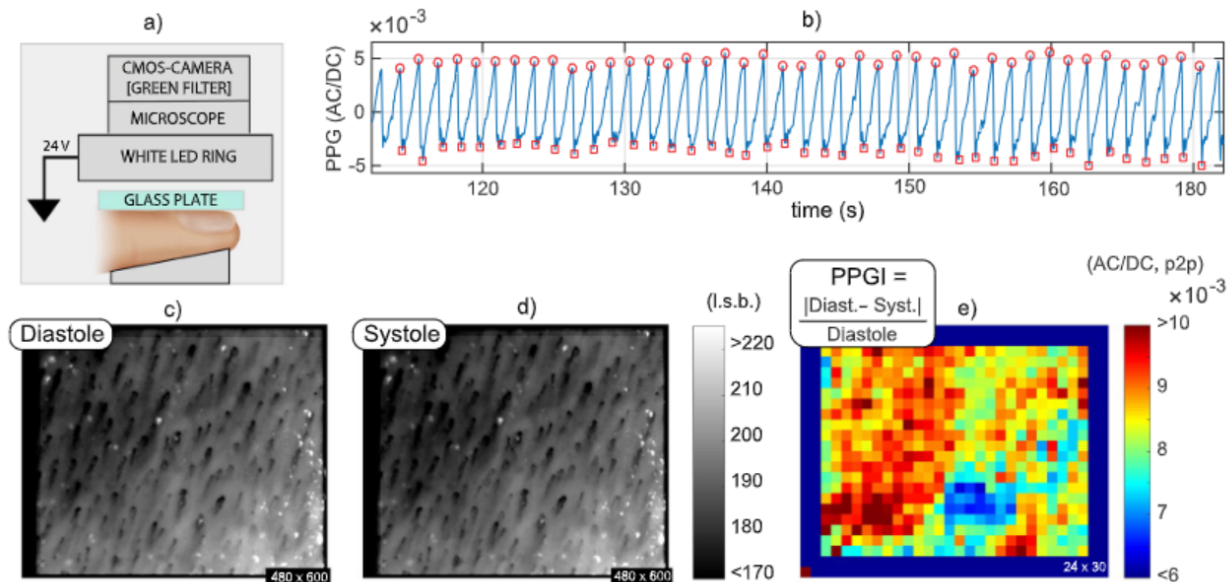


图4. 使用绿色波长对指甲褶皱进行视频毛细血管镜检查：(a) 设置示意图；(B) 平均PPG信号，指示收缩期最大值（圆圈）和最小值（正方形）；以及分别在(c) 峰瞬间和(d) 谷值时上层真皮的超分辨率图像（成像面积，约 1.6×2 mm 2 ；放大倍数， $\times 60$ ）。(c, d) 之间的缩小和归一化的差分像是PPG图像(e)，其表明毛细血管密度和PPG信号强度之间没有关系。这个图形是由A.莫索

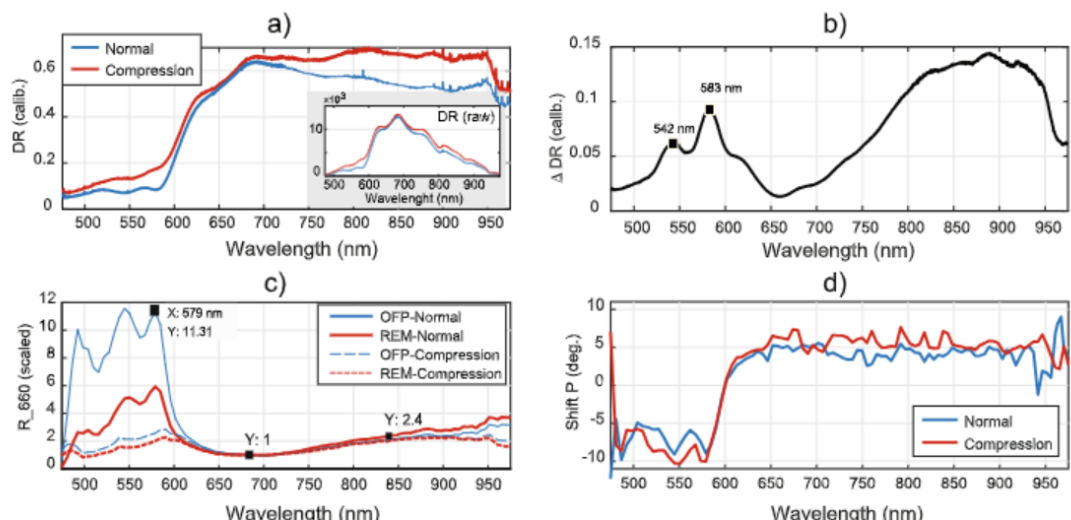


图5. (a) 在皮肤压缩之前和在皮肤压缩下测量的DR曲线；(b) DR差异证明氧合血红蛋白吸收峰。通过压缩在维斯(<580 nm)范围内消除PPG，见(c) 缩放PPG幅度测量(R_{660} ; OFP, 光纤探头; REM, 远程PPG)。(d) PPG-相位光谱在约600 nm处移位，这表明维斯和IR之间的形状不相似。

图5c示出了在正常和受压皮肤($N = 15$)处用光度计-OFP系统获得的PPG光谱的中值。还包括通过使用传递函数(TF)估计的相应远程光谱，该传递函数考虑了皮肤特性和探头规格(有关详细信息，请参见方法部分)。为了便于比较，PPG振幅光谱通过其在660 nm处的相对最小值进行缩放，并定义了两个变量：绿色相对于红色的振幅比(戈尔，绿色和红色范围分别定义在520-577 nm和660-700 nm处)，以及IR(范围，800-840 nm)相对于红色的比率(IRoR)。在我们的数据集中，配对样本t检验表明，压缩显著降低了平均戈尔的4倍(平均值±标准差；参考值， 927 ± 319 ；压缩值， 2.32 ± 1.24 ；1个拒绝离群值； $p < 0.001$)，而IRoR未受到显著影响(参考， 1.90 ± 0.16 ；压缩， 1.95 ± 0.14 ； $p = 0.43$)。这通过证明选择性阻断真皮层影响浅PPG-绿色波长来支持多层BVV假设。请注意，IRoR对压缩的不变性适用于远程采集，因为探头几何结构不相关。

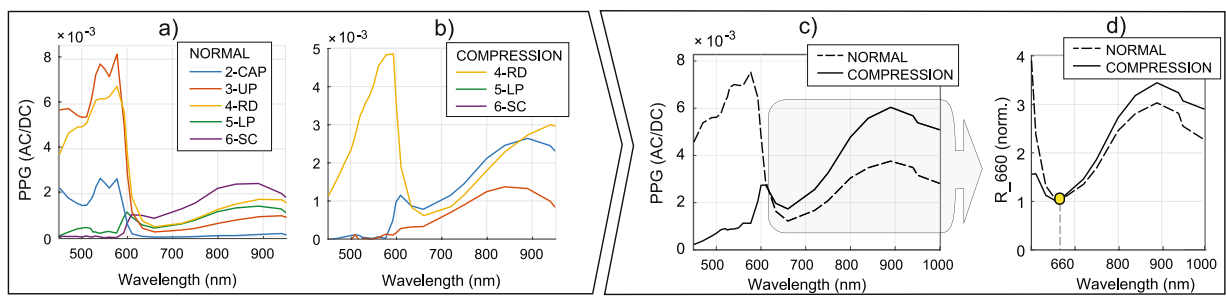


Figure 6. Skin layers signatures simulated for (a) reference and for (b) compression conditions, evidencing that deeper layers contribute the least to PPG in blue-green. Upon linear combination with weights w_{ref} and w_{comp} the remote PPG spectra are provided as (c) AC/DC and (d) relative to the amplitude at 660 nm.

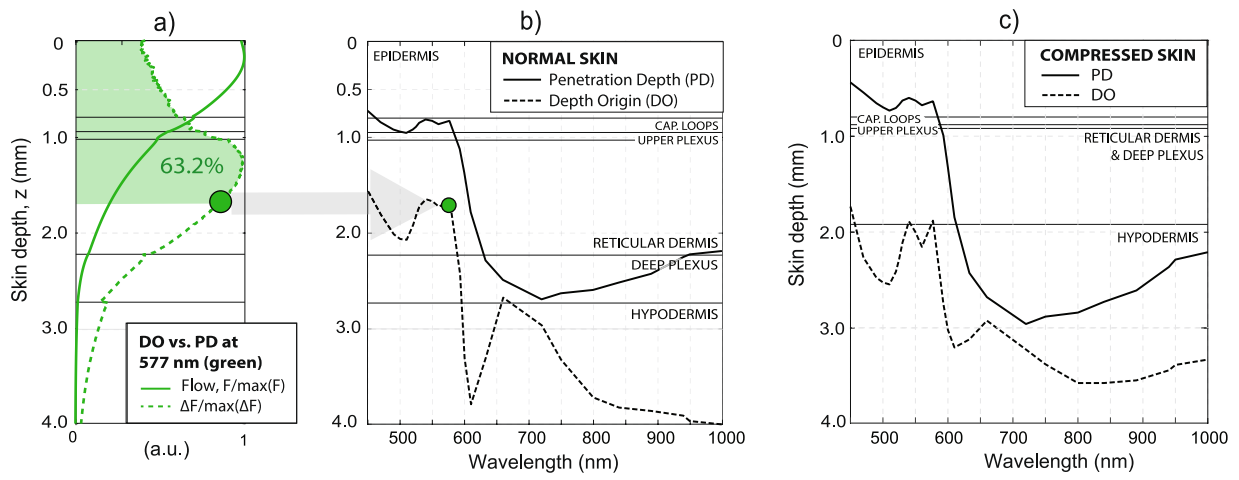


Figure 7. Comparison of the penetration depth (PD) of the incident light at the skin against the depth-origin (DO) of PPG for (a,b) normal and (c) compressed skin, showing that PPG modulations reach pulsating layers and have arteriolar origin in VIS-IR. As exemplified for 577 nm, the PD is determined as 63.2% of the area under the diastolic or systolic flow curves since $F^{(d)} \approx F^{(s)}$. Analogously, the DO of PPG is calculated from the diastolic-systolic difference $\Delta F = |F^{(d)} - F^{(s)}|$.

in the red-IR diagnostic window. That green and red-IR wavelengths probe different mixture-weights of the layers signatures explains the selective mitigation of the PPG-amplitude below 580 nm by compression.

Figure 5d contrasts the relative PPG-phase shift spectra in the 475–975 nm wavelength range. The dual-state behaviour of the relative PPG-phase function, with stable phases within the blue-green (475–580 nm) and red-IR (625–975 nm), means that the shapes of the PPG signals are fairly similar within the ranges. The phase gap at ~600 nm indicates the abrupt penetration depth change, which is influenced slightly by the compression-induced blanching of the skin.

Experimental Part 2: Monte Carlo simulations. The simulated layer's signatures for normal and compressed skin are depicted in Fig. 6(a,b). The simulated remote PPG spectra resemble measurements for, e.g., pulsation patterns of $w_{ref} = (0, 0, 1, 2, 3, 1)/3$ and $w_{comp} = (0, 0, 0, 2, 18, 1)/3$, for layers (1-EPI, ..., 6-SC), for reference and compression, respectively.

The simulations for the penetration depth (PD) and depth-origin (DO) of the PPG signals are insightful to assess if arteriolar BVVs can, at least theoretically, modulate PPG. Figure 7a exemplifies the light flux, $F(z)$, and differential flux between diastole and systole, $\Delta F(z)$, for 577 nm. The PD is defined as the depth for which area under $F(z)$ is ~63.2%. Analogously, the DO is defined as the depth for which the area under $\Delta F(z)$ is ~63.2%.

In agreement with earlier work^{15,23}, we verified that the PD of blue-green wavelengths is at the level of the capillary loops (see Fig. 7b). However, only a small fraction of the diffusely reflected photons need to be modulated for PPG signal generation. The DO for the reference skin model is greater than the PD. This means that PPG in VIS effectively reaches the pulsating arterioles of the upper plexus and the RD. These insights also hold in IR; i.e., the center of gravity of the DO of the PPG signals in VIS-IR is deeper than the PD of the incident light. Similar insights hold for the compressed skin model (see Fig. 7c).

Discussion

This investigation aims to assess if the opto-physiology of remote PPG in VIS-IR can be explained by arteriolar/arterial BVVs located at dermal and subdermal skin layers. Using the finger pad as inspection site, we showed

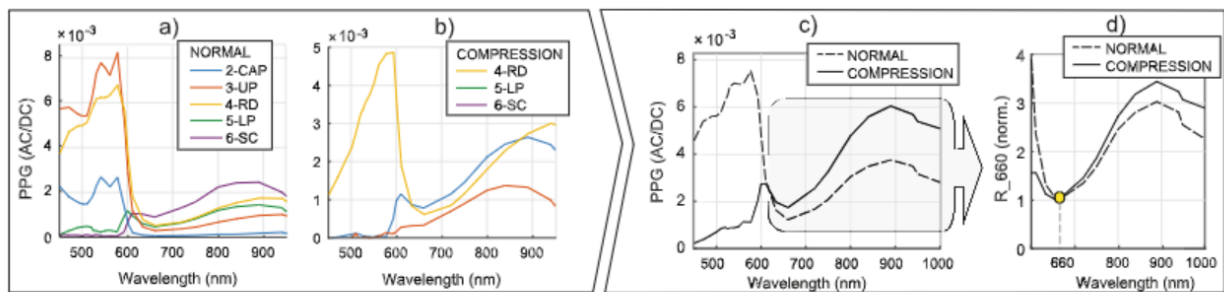


图6.针对 (a) 参考和 (B) 压缩条件模拟的皮肤层特征，证明较深层对蓝绿色PPG的贡献最小。在与权重w和w进行线性组合时，远程PPG光谱被提供为 (c) AC/ DC和 (d) 相对于660 nm处的振幅。

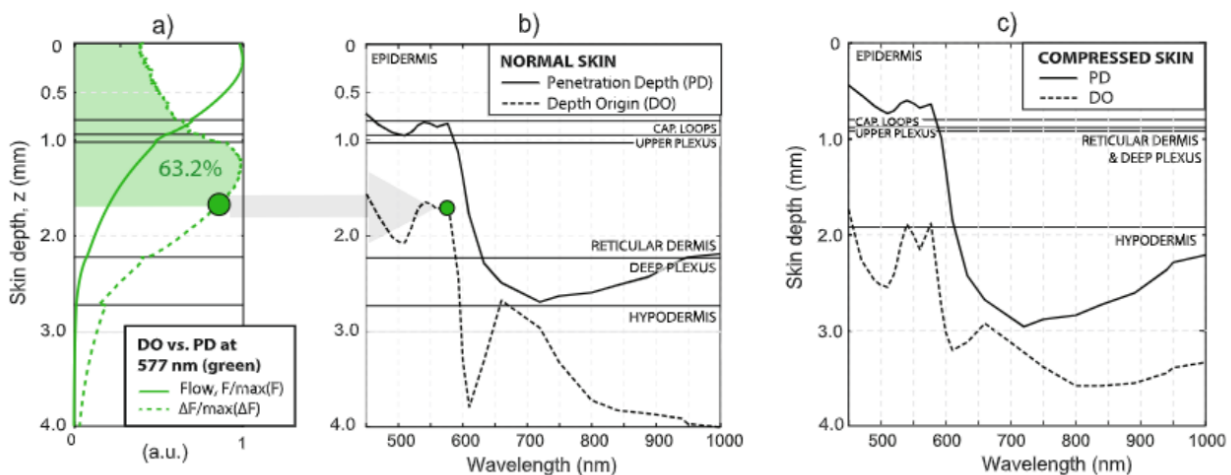


图7.对于 (a, B) 正常皮肤和 (c) 压缩皮肤，将入射光在皮肤处的穿透深度 (PD) 与PPG的深度原点 (DO) 进行比较，表明PPG调制到达脉动层并且在VIS-IR中具有小动脉原点。如对于577 nm所例示的，PD被确定为自F → F起的舒张或收缩流量曲线下的面积的63.2%。类似地，PPG的DO由舒张压-收缩压差 $\Delta F = |F - F'|$.

红色红外诊断窗口绿色和红色IR波长探测层特征的不同混合权重解释了通过压缩对低于580 nm的PPG幅度的选择性减轻。

图5d对比了475-975 nm波长范围内的相对PPG相移光谱。相对PPG相位函数的双态行为，在蓝-绿（475-580 nm）和红-IR（625-975 nm）内具有稳定相位，意味着PPG信号的形状在范围内相当相似。在~600 nm处的相隙指示突然的穿透深度变化，其轻微地受皮肤的压缩诱导的漂白的影响。

实验部分2：蒙特卡罗模拟。图6 (a, B) 中描绘了正常皮肤和压缩皮肤的模拟层的签名。模拟的远程PPG谱类似于例如以下的测量：对于层 (1- EPI, ..., 6- SC)，分别为参考和压缩的 $w= (0, 0, 1, 2, 3, 1) / 3$ 和 $w= (0, 0, 0, 2, 18, 1) / 3$ 的脉动模式。

PPG信号的穿透深度 (PD) 和深度原点 (DO) 的模拟对于评估小动脉BVV是否可以（至少在理论上）调节PPG具有重要意义。图7a显示了577 nm时的光通量 $F(z)$ 以及舒张期和收缩期之间的光通量差 $\Delta F(z)$ 。PD定义为 $F(z)$ 下面积约为63.2%的深度。类似地，DO定义为 $\Delta F(z)$ 下面积约为63.2%的深度。

与早期的工作一致，我们证实了蓝绿色波长的PD处于毛细血管环的水平（见图7b）。然而，仅漫反射光子的一小部分需要被调制以用于PPG信号生成。参考皮肤模型的DO大于PD。这意味着维斯中的PPG有效地到达上从和RD的脉动小动脉。这些见解也适用于IR；即，在VIS-IR中PPG信号的DO的重心比入射光的PD深。类似的见解适用于压缩皮肤模型（参见图7c）。

讨论情况

本研究旨在评估VIS-IR中远程PPG的光生生理学是否可以通过位于真皮和皮下皮肤层的小动脉/ 动脉BVV来解释。使用指垫作为检查部位，我们发现

that the remote PPG-amplitude spectrum for normal and for compressed skin can be acquired and modeled in light of the volumetric model. Skin compression reduces the blood content of the skin (particularly venous blood) and enables that green wavelengths penetrate deeper and reach more pulsating vessels. Since the depth-origin of the PPG signals is within the arteriolar level in VIS and IR, an alternative model for the genesis of PPG in VIS is, therefore, unnecessary. Yet, we remark that our insights are not direct experimental evidence and do not invalidate the possibility of complementary mechanisms of PPG formation occurring in parallel.

The volumetric model holds for all skin sites but the PPG spectra have skin-site variations. Our preliminary results suggest lower overall PPG-amplitudes and an imbalance between amplitudes in green versus red-IR wavelengths, for glabrous and non-glabrous skin (see Section 2 in the Supplementary file). Possible explanations include density of arterio-venous shunt density, microvascular bed thickness and epidermal scattering and absorption.

To the best of our knowledge, only Reuss²² stated explicitly that the capillary loops are microcirculatory, but there is no experimental support for this assumption. At most, capillary flow velocities can be estimated and shown to have a constant and a pulsatile component. Based on nailfold videocapillaroscopy, the typical RBC average velocity measured in healthy subjects is around $0.8 \pm 0.2 \text{ mm/s}$ ²⁷. More recently, Baran *et al.*²⁸ applied Doppler optical microangiography (DOMAG) method to map RBC absolute velocity in the arterial and side of the finger cuticle capillaries loops and obtained about 0.67 mm/s for arteriole-end capillaries. Unfortunately, the sampling rate was limited to 0.5 frames per minute, which did not allow the assessment of pulsating flow inside the capillary loops. Still, the fact that RBC speed even reduces in capillary loops²⁸ with increasing flow resistance at low velocities²⁹ suggests the steadiness of blood flow at upper arterioles. The assumption of constant flow velocity at the capillaries is not subscribed by Huelsbusch²³, who modeled PPG assuming that the PPG is formed at the capillary loops only. Interestingly, Huelsbusch's simulated spectrum largely overestimates the magnitude of signals in blue-green wavelengths, suggesting the incorrectness of this parameter setting. We verified that the problem does not occur in simulations where the sources of pulsatility/BVVs are at the dermal plexuses, RD and SC.

Recently, Volkov *et al.*³⁰ showed that the capillary flow speed of RBCs of the fingernail fold have a pronounced pulsatile flow component overlapped with an asynchronous component. The magnitude of the capillary flow speeds (range, $1\text{--}5 \text{ mm/s}$) is dissonant from reference healthy ranges, but the observed morphological resemblance between capillary flow speed waveforms and pulsatile blood pressure waveforms is invariant to possible scaling inaccuracies. Still, these waveforms were erroneously interpreted as evidence for the inadequacy of volumetric theory. In fact, if the data of Volkov *et al.* is valid, then any remnants of pulsatile pressure that reach the capillary level are accommodated as pulsatile flow and not as capillary BVVs. This possibility is strengthened by morphological resemblance between Volkov's flow speed waveforms and the pulsatile pressure waveforms of Mahler *et al.*³¹, who performed direct cannulation of human finger nailfold capillaries.

Limitations and future work. *Modeling simplifications.* We begin by acknowledging the simplifying assumption of a reference skin model and PPG spectrum. This exercise should only hold for illustrative purposes because PPG is highly influenced by individual and contextual factors like posture³² and skin site (see Section 2 in the Supplementary file for details). Additional skin models with slight changes in the layers properties, e.g., thickness, relative pulsatile strength and absorption, would add to this study by translating inter-individual and skin-site variations. Still, building and running these come at the cost of added computational effort and time while a single skin model suffices to verify that the normal and compressed PPG-amplitude spectra are obtained for realistic parameter settings.

We further remark that modeling the skin as a structure with a discrete number of stacked horizontal layers is a valid simplification³³, though not without the possible risk that the microanatomic description of the skin into 2 plexuses may not be representative of all skin sites^{34,35}. Wong and Geyer visualized the finger pad using optical coherence tomography (OCT) and documented a tree-like ramification where relatively thick dermal arteries arise from the subcutaneous arterial plexus and ramify until they form the ascending segment of the capillary loops. As reported, capillary loops of the finger pad could be split in "arterial units" and the upper plexus would be absent. However, the volumetric model for PPG signal formation also holds if the skin microvasculature has a tree-like arrangement, although the mixing weights of the layer contributions to the resulting PPG spectrum may differ at the upper dermis. Future work is valuable to ascertain these considerations.

Parameter errors. Selecting optical parameters from the literature is an error-prone task. Glaring examples are the absorption and scattering parameters, which are mostly determined in *ex vivo* tissue samples and may differ by an order of magnitude^{36,37}. Moreover, the scattering coefficients of living skin can be much lower than those of *ex vivo* samples^{38,39}.

Although the major findings are not affected, the uncertainty in parameter settings influences the DRS and PPG spectra. The computation of the skin layer's signatures is robust to small variations in blood concentration at the upper dermis. However, the same does not hold if the skin layers scattering or absorption coefficients vary by an order of magnitude. Figure 8 exemplifies the considerable impact on spectral simulations of an hypothetical variation in epidermal scattering by an order of magnitude (reference $\mu_{s,EPI} = 156.34 \text{ cm}^{-1}$ versus reduced $\mu_{s,EPI} = 10.42 \text{ cm}^{-1}$; common parameters for the epidermal layer: $n = 1.33$; $\mu_{a,EPI} = 15.039$; $g = 0.9$; $d_{EPI} = 0.8 \text{ mm}$).

The errors incurred in parameter settings do not preclude the remote PPG spectrum from being obtained. However, the errors propagate to the mixing weights of the BVVs. Consequently, the inverse estimation of the mixing weights of the BVVs is currently an ill-posed problem. Future progresses in this direction could enable the possible usefulness of the skin's pulsating profile for functional tissue characterization.

Probe effects. DR measurements were contact-based and may contain probe pressure artifacts^{40,41}. Concerns are rested by verifying that the DR plot for the non-compressed skin is similar to those of Bjorgan *et al.*⁴². Probe

可以根据体积模型来采集和建模正常皮肤和受压皮肤的远程PPG幅度谱。皮肤压缩减少了皮肤的血液含量（特别是静脉血），并且使得绿色波长能够穿透得更深并且到达更多的脉动血管。由于PPG信号的深度原点在维斯和IR中的小动脉水平内，因此不需要维斯中PPG起源的替代模型。然而，我们注意到，我们的见解不是直接的实验证据，并没有使并行发生的PPG形成的互补机制的可能性无效。

体积模型适用于所有皮肤部位，但PPG频谱具有皮肤部位变化。我们的初步结果表明，对于无毛和非无毛皮肤，总体PPG振幅较低，并且绿色与红色IR波长的振幅之间不平衡（参见补充文件中的第2节）。可能的解释包括动静脉分流密度、微血管床厚度和表皮散射和吸收。

据我们所知，只有Reuss明确指出毛细血管袢是微循环的，但没有实验支持这一假设。最多，毛细血管流速可以估计和显示有一个恒定的和脉动的组件。基于甲襞视频毛细血管镜检查，在健康受试者中测量的典型RBC平均速度约为 $0.8 \pm 0.2 \text{ mm/s}$ 。最近，Baran等人应用多普勒光学微血管造影(DOMAG)方法来绘制动脉和手指表皮毛细血管环侧中的RBC绝对速度，并获得了约 0.67 mm/s 的小动脉末端毛细血管。不幸的是，采样率被限制为每分钟0.5帧，这不允许评估毛细血管环路内的脉动流。尽管如此，红细胞速度甚至在毛细血管环中降低，在低速度下流动阻力增加，这一事实表明上部小动脉的血流稳定。Huelsbusch不同意毛细血管处恒定流速的假设，他对PPG进行了建模，假设PPG仅在毛细血管环路处形成。有趣的是，Huelsbusch的模拟光谱在很大程度上高估了蓝绿色波长的信号幅度，这表明这个参数设置是不正确的。我们验证了在脉动/BVV源位于真皮丛RD和SC的模拟中不会发生该问题。

最近，Volkov等人表明，指甲褶RBC的毛细血管流速具有明显的脉动流分量，与异步分量重叠。毛细血管流速的幅度（范围， $1\text{-}5 \text{ mm/s}$ ）与参考健康范围不一致，但观察到的毛细血管流速波形和脉动血压波形之间的形态相似性对于可能的缩放不准确性是不变的。尽管如此，这些波形被错误地解释为体积理论不足的证据。事实上，如果Volkov等人的数据有效，则到达毛细血管水平的任何残余脉动压力均被视为脉动流，而不是毛细血管BVV。Volkov的流速波形和Mahler等人的脉动压力波形之间的形态相似性加强了这种可能性，Mahler等人进行了人手指甲襞毛细血管的直接插管。

局限性和今后的工作。模型简化。我们开始承认参考皮肤模型和PPG谱的简化假设。该练习仅用于说明目的，因为PPG受个体和背景因素（如姿势和皮肤部位）的影响很大（详细信息请参见补充文件中的第2节）。层属性略有变化的其他皮肤模型，例如，厚度、相对脉动强度和吸收将通过转换个体间和皮肤部位变化而增加到该研究中。尽管如此，构建和运行这些是以增加计算工作量和时间为代价的，而单个皮肤模型足以验证针对现实参数设置获得正常和压缩PPG幅度谱。

我们还注意到，将皮肤建模为具有离散数量的堆叠水平层的结构是有效的简化，尽管并非没有可能的风险，即皮肤的2个神经丛的显微解剖描述可能不代表所有皮肤部位。Wong和盖耶使用光学相干断层扫描(OCT)对指垫进行了可视化，并记录了树状分支，其中相对较厚的真皮动脉从皮下动脉丛发出，并分叉，直至形成毛细血管袢的上升段。据报道，指垫的毛细血管袢可以分裂成“动脉单位”，而上丛将缺失。然而，如果皮肤微脉管系统具有树状布置，则用于PPG信号形成的体积模型也成立，尽管层对所得PPG谱的贡献的混合权重在上层真皮处可能不同。今后的工作对确定这些考虑是有价值的。

参数错误。从文献中选择光学参数是一项容易出错的任务。引人注目的例子是吸收和散射参数，其主要是在离体组织样品中确定的，并且可能相差一个数量级。此外，活体皮肤的散射系数可以比离体样品的散射系数低得多。

虽然主要发现不受影响，但参数设置的不确定性会影响DRS和PPG光谱。皮肤层的签名的计算对于上层真皮处的血液浓度的小变化是鲁棒的。然而，如果皮肤层散射或吸收系数变化一个数量级，则情况并非如此。图8以一个数量级（参考 $\mu = 156.34 \text{ cm}$ vs降低 $\mu = 10.42 \text{ cm}$;表皮层的常见参数： $n = 1.33$; $\mu = 15.039$; $g = 0.9$; $d = 0.8 \text{ mm}$ ）说明了表皮散射假设变化对光谱模拟的显著影响。

参数设置中产生的误差不妨碍获得远程PPG频谱。

然而，误差传播到BVV的混合权重。因此，BVV的混合权重的逆估计目前是一个不确定问题。在这个方向上的未来进展可能使皮肤的脉动轮廓的功能组织表征的可能有用。

探针效应。DR测量是基于接触的，可能包含探头压力伪影。通过验证非压缩皮肤的DR图与Bjorgan等人的DR图相似，消除了顾虑。探针

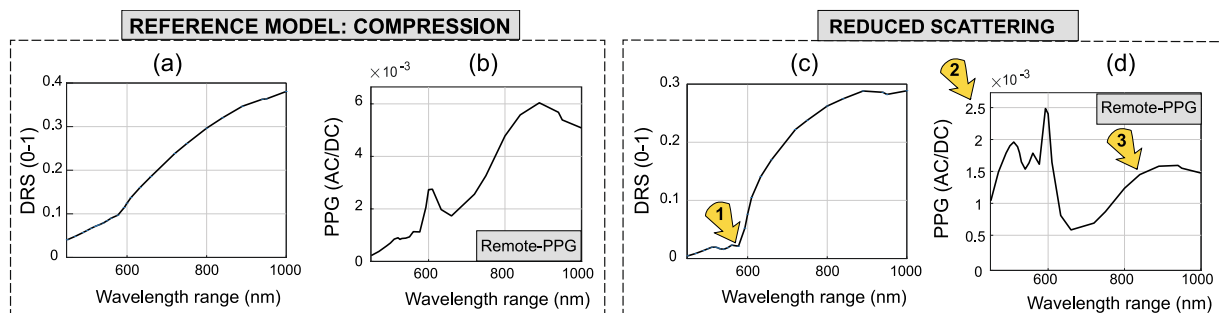


Figure 8. Spectral effects due to uncertainty in the epidermal scattering coefficient. **(a,b)** Baseline $\mu_{s,EPI} = 156.34\text{ cm}^{-1}$ versus **(c,d)** Alteration $\mu_{s,EPI} = 10.42\text{ cm}^{-1}$. The yellow flags point to differences in 1. DR at green wavelength range, and 2,3 PPG-amplitude magnitude and ratio between blue-green versus red-IR windows.

effects reduce the PPG-amplitude ratios in green over red-IR by a factor of up to 0.7 (corresponding to about 1 mm of finger compression; see Supplementary section 1 for details on the PPG-amplitude response to incremental finger pad compression in green and IR). Modeling the geometry of the OFP (implicit in TF computations) is another possible source of error which makes it inviting to perform of spectral measurements remotely as demonstrated by Corral *et al.*⁴³ and Blackford *et al.*⁴⁴. However, measuring the PPG spectra in reflectance-mode was preferable to remote multispectral measurements since the latter are noisier. Concerns to the validity of the remote spectra PPG include ballistocardiographic artifacts¹⁷ and specular reflections.

Conclusion

The exploration of the VIS range in PPG-based applications is relatively recent and the underlying opto-physiology remains doubtful. Our results present a step forward in this regard by supporting the volumetric model. By taking a joint numerical and experimental approach, we linked the skin's pulsating profile and signatures at different skin-depths with the remote PPG-amplitude spectrum. Our results support that arteriole-arterial BVVs are feasible as origin of PPG signals in visible light and IR. The depth-origin of PPG using green wavelengths are dermal BVVs while red-IR wavelengths even interact with subcutaneous BVVs. The videocapillaroscopic mapping of the PPG-amplitude at the finger nail fold further suggests that the PPG signal is not associated with capillary density.

Methods

Participants. Sixteen subjects (ages, 27–55 years old; 2 females) participated in this investigation. The study was approved by the Internal Committee Biomedical Experiments of Philips Research and an informed consent was obtained from each subject. All experiments were carried out in accordance with the ethical standards laid down in the 1964 Declaration of Helsinki.

Data acquisition. We explored three modalities for acquiring skin reflectance data. Camera-based remote PPG measurements were made in green versus IR bands. Because of its relevance for prospective PPG-imaging applications, the derived insights are the foundation of this study. Videocapillaroscopy offers a joint morphological and functional assessment of the upper dermis and of the associated remote PPG signal strength. DRS extends insights to the 500–940 Hz spectra, and strengthens our study by making the skin compression intervention possible.

This section details the data acquisition settings used in this investigation. We highlight that, in all data acquisition modalities, the sampling rates in the range 16–30 Hz are well above the Nyquist frequency (about 1 Hz) and enable estimating the average pulse-rate frequency using Fourier analysis in each temporal window of 10–20 sec. The average diastole and systole instants are determined with a precision error of 63 ms, which is appropriate for noise mitigation and imaging PPG.

Camera-based remote PPG measurements. Skin video recordings were performed using a monochrome camera (IDS Inc, Germany; model μEye, UI122xSE-M; 12 bit resolution; model, USB 2000+; sampling rate, 20 or 30 Hz). The susceptibility of remote PPG to motion artifacts was addressed in finger pad recordings by supporting the forearm on a table. Additional care was taken to eliminate specular reflections by including polarizing film in front of the light source and camera in a cross-polarization arrangement. For each video recording, skin regions of interest (sRoIs) were manually demarcated at video recordings of the finger pad and used to extract PPG signals. For each frame, the raw PPG signal is computed by averaging the time-varying intensity of the sRoI in successive frames. Each camera channel retrieves a single time series per sRoI.

Videocapillaroscopy. Recordings were performed at the finger nail fold of one subject from our dataset. Our system comprised a CMOS camera (coupled with a green filter; sampling rate, 20 Hz), a microscope lens (magnification factor, 40x) and a white high power LED ring light (CCS HPR2-100SW; fluorescent white; voltage, 24 VDC; see Fig. 4a). Motion artifacts were addressed by supporting the forearm on a table. Minute cardiac-related bulk motion cannot be fully suppressed, but the diffuse lighting at the imaged finger nailfold prevents artifacts in remote PPG signals and amplitude maps. Specular reflections were minimized by applying a thin layer of

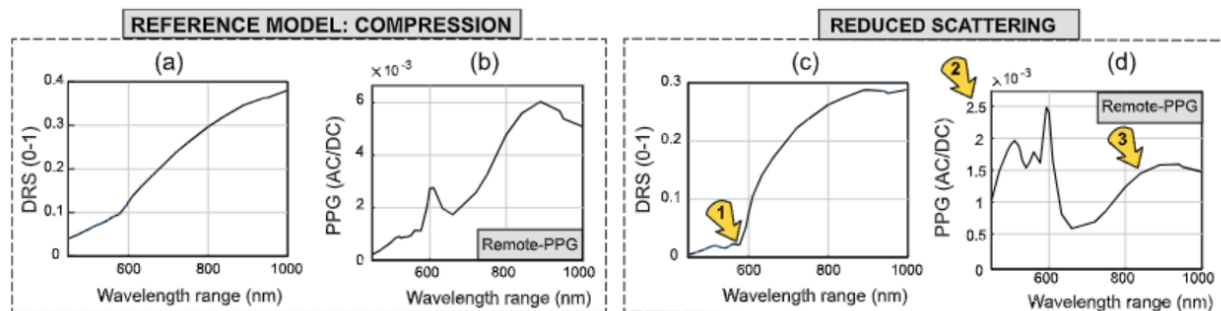


图8.表皮散射系数不确定性引起的光谱效应。(a, B) 基线 $\mu = 156.34 \text{ cm}$ 对比(c, d)变化 $\mu = 10.42 \text{ cm}$ 。黄旗表示1中的差异。在绿色波长范围的DR, 以及2, 3 PPG-振幅幅度和蓝-绿色与红-IR窗口之间的比率。

效应使绿色中的PPG幅度比相对于红色-IR降低高达0.7倍（对应于约1 mm的手指压缩，关于对绿色和IR中的递增指垫压缩的PPG幅度响应的细节，参见补充部分1）。对OFP的几何形状进行建模（在TF计算中隐含）是另一个可能的误差来源，这使得它吸引了远程执行光谱测量，如Corral等人和布萊克福德等人所证明的。然而，在反射模式下测量PPG光谱优于远程多光谱测量，因为后者噪声更大。对远程频谱PPG的有效性的关注包括心冲击描记伪影和镜面反射。

结论

在基于PPG的应用中对维斯范围的探索是相对较新的，并且潜在的光生理学仍然值得怀疑。我们的研究结果提出了一个步骤，在这方面的支持体积模型。通过采取联合数值和实验方法，我们将皮肤的脉动轮廓和不同皮肤深度的签名与远程PPG幅度谱联系起来。我们的研究结果支持动脉BVV作为可见光和IR中PPG信号的起源是可行的。使用绿色波长的PPG的深度起源是皮肤BVV，而红色-IR波长甚至与皮下BVV相互作用。在指甲褶皱处的PPG幅度的视频毛细血管镜映射进一步表明PPG信号与毛细血管密度无关。

方法

参与者 16名受试者（年龄，27 - 55岁；2名女性）参加了本研究。本研究获得Philips Research 生物医学实验内部委员会的批准，并获得每例受者的知情同意书。所有实验均按照1964年赫尔辛基宣言中规定的伦理标准进行。

数据采集。我们探讨了三种方式获取皮肤反射数据。在绿色与IR波段中进行基于相机的远程PPG测量。由于其与前瞻性PPG成像应用的相关性，因此得出的见解是本研究的基础。视频毛细血管镜检查提供了一个联合的形态和功能评估上层真皮和相关的远程PPG信号强度。DRS将见解扩展到500 - 940 Hz频谱，并通过使皮肤压缩干预成为可能来加强我们的研究。

本节详细介绍了本调查中使用的数据采集设置。我们强调，在所有数据采集模式中，16-30 Hz范围内的采样率远高于奈奎斯特频率（约1 Hz），并且能够在10-20秒的每个时间窗口中使用傅立叶分析来估计平均脉搏率频率。以63 ms的精度误差确定平均舒张和收缩时刻，这适用于噪声缓解和成像PPG。

基于相机的远程PPG测量。使用单色相机（IDS Inc, 德国;型号μEye, UI 122 xSE-M; 12位分辨率;型号USB 2000+;采样率, 20或30 Hz）进行皮肤视频记录。通过将前臂支撑在桌子上，在指垫记录中解决了远程PPG对运动伪影的敏感性。通过在交叉偏振布置中的光源和相机前面包括偏振膜来额外注意消除镜面反射。对于每个视频记录，在指垫的视频记录处手动划分感兴趣的皮肤区域（sROI），并用于提取PPG信号。对于每帧，通过对连续帧中sROI的时变强度求平均来计算原始PPG信号。每个摄像机通道检索每个sROI的单个时间序列。

视频毛细血管镜检查。在我们数据集中的一个受试者的指甲褶皱处进行记录。我们的系统包括CMOS相机（与绿色滤波器耦合;采样率, 20 Hz）、显微镜透镜（放大倍数, 40 x）和白色高功率LED环形灯（CCS HPR 2 - 100 SW;荧光白色;电压, 24 VDC;参见图4a）。通过将前臂支撑在桌子上来解决运动伪影。无法完全抑制与心脏相关的微小体运动，但成像手指甲襞处的漫射照明可防止远程PPG信号和振幅图中的伪影。镜面反射最小化，通过施加一层薄薄的

ultrasound gel at the nail fold and a microscope slide, which promote the translucency of the epidermis (refractive index = 1.3) and by using a LED-ring close to the finger site (distance of about 1 cm). The orientation of the LEDs (70–80 degrees w.r.t. the camera, which is frontal to the nailfold) helped to minimize specular reflections. The observation that PPG originates from non-capillary regions within videocapillaroscopic data and the derived PPG-amplitude images was confirmed in different measurement sessions and fingers.

DRS. Contact-based reflectance data was probed with a spectrometer (Ocean Optics, Inc.; model, USB 2000+; 12 bit resolution; software, SpectraSuite, 2008) coupled with an OFP. For each recording, we obtained parallel sets of $N=2048$ time series at collocated, narrow and non-overlapping frequency bands, including the 475–975 nm range. The OFP (diameter, 400 μm) was shielded by a cylindrical ferrule which blocked ray paths back-scattered up to 1.59 mm from its center.

The finger pressures applied with our DRS-OFP equipment at normal/reference measurement conditions at the finger pad are low and estimated to be below 10 kPa (finger compression depth, below 1 mm). In contrast, the applied pressure intensity used for eliciting the compression regime in the DRS reference-compression intervention is estimated to be within about 40 to 60 kPa (compression depth, about 2 mm). These compression estimates were based on a devoted experiment of PPG-amplitude and DR measurements under gradually increasing finger pad compression (see Supplemental Section 1).

Processing skin reflectance data. Our experimental data is raw skin reflectance (sampled well above the pulse-rate frequency) from which we aim to ensemble PPG signals. The nuances in signal processing requirements for camera-based PPG acquisition and DRS are described below.

Camera-based video recordings. Raw PPG signals in video recordings were extracted by averaging pixels in user-defined sROIs and AC/DC-normalized (i.e., divided by its slowly-varying component, obtained with low-pass-filtering with a Butterworth filter with cutoff frequency at ~40 bpm). The amplitude of the reflection-mode PPG signals is typically low (particularly in red wavelengths), but its signal-to-noise ratio (SNR) can be improved by adaptive bandpass filtering (ABPF). ABPF consists of filtering out the frequency components of the signals that are not multiples of the fundamental of the pulse-rate frequency.

ABPF was applied in an overlap-and-add manner (stride length, 256 samples; overlap factor, 50%) with Hanning windowing. We selected the fundamental and 6 harmonics of the pulse-rate frequency and a tolerance band of one bin around each center frequency. When available, the reference signals used for identifying the systolic peaks and instantaneous pulse-rate were finger pulse oximetry signals (acquired synchronously with video recordings). Alternatively, the reference were the PPG-signals probed at green wavelengths, as these have the best available SNR. After ABPF, the PPG cycles in streams were condensed into ensemble-averaged (EA) waveforms, separately for each camera channel and signal dimension. EA relies on Gaussian noise cancelation in the averaging process and in the signals periodicity. In practice, cycles were demarcated based on the timing of the systolic peaks (identified in reference signals), temporally registered, and, finally, averaged by using the trimmed mean operator (outlier rejection, 10%). Each super-resolved EA waveform condenses, at least, 100 consecutive cycles.

Processing of DRS recordings. As a preprocessing step, DRS streams require calibration for additive sensor noise. This is done by subtracting the noise floor in each wavelength, λ . By denoting the raw reflectance as $DR_0(t, \lambda)$, its calibration is expressed as

$$DR(t, \lambda) = \frac{DR_0(t, \lambda) - DR_{DARK}(\lambda)}{DR_{REF}(t, \lambda) - DR_{DARK}(\lambda)}, \quad (1)$$

where $DR_{DARK}(\lambda)$ denotes the noise level in full darkness. Similarly, $DR_{REF}(\lambda)$ denotes the reflectance measurement of a reference standard (model WS-1, reflectivity >98% from 250–1500 nm, Ocean Optics, Inc.) placed frontally to the OFP at a distance of 2 mm. DR recordings were processed to obtain reflectance PPG-amplitude and PPG-phase spectra.

Monte Carlo simulations of skin reflectance and remote PPG. The spectrum and depth-origin of remote PPG was simulated by the Monte Carlo method. These efforts were preceded by Huelsbusch²³, but his assumption that the remote PPG signal comes exclusively from the capillary loops, as well as his overestimated blood concentration and scattering coefficients of the skin, resulted in the underestimation of PPG signals in red-IR. We overcame these issues using parameters from the DRS literature and/or estimated based on our experiments. We simulated the photon migration through the tissue for the diastolic and systolic states at a set of tissue characteristics, including SpO_2 and blood concentration in the tissue, where the systolic state was obtained by an incremental increase of arterial blood over the diastolic state. Data were computed over multiple skin layers and in the 450–1000 nm range.

We used the publicly available GPU-MCML code package, which enables simulating photon propagation in a multi-layered turbid media with adjustable spatial dimensions and resolution⁴⁵. The geometry of the scenario is specified in cylindrical coordinates with the emitter centered at the origin and normal to the tissue surface³³. The emitter configuration approximates collimated light from an infinitely narrow beam. The input (.mci) files for MCML incorporated skin architecture parameters, absorbance and scattering coefficients, and physiological parameters such as SpO_2 , blood concentration, melanin content, etc. Separate models were implemented for reference and compressed skin.

超声波凝胶在指甲褶皱和显微镜载玻片，这促进了表皮的透明性（折射率=1.3），并通过使用LED环接近手指部位（距离约1厘米）。LED的方向（相对于LED的70-80度）位于甲襞前方的照相机有助于最小化镜面反射。在不同的测量会话和手指中证实了PPG源自视频毛细血管镜数据内的非毛细血管区域的观察结果和导出的PPG振幅图像。

基于接触的反射率数据用分光计（Ocean Optics, Inc.;型号，USB 2000+; 12位分辨率;软件，SpectraSuite，2008）。对于每个记录，我们获得了N = 2048个时间序列的并行集合，在并置的，窄的和不重叠的频带，包括475-975 nm范围。OFP（直径400 μm）由圆柱形套圈屏蔽，该套圈阻挡从其中心向后散射达1.59 mm的射线路径。

在正常/参考测量条件下，我们的DRS-OFP设备在指垫处施加的手指压力较低，估计低于10 kPa（手指按压深度，低于1 mm）。相比之下，用于在DRS参考按压干预中引发按压方案的所施加的压力强度估计在约40至60 kPa（按压深度，约2 mm）内。这些压缩估计值基于逐渐增加指垫压缩下PPG振幅和DR测量的专门实验（见补充章节1）。

处理皮肤反射数据。

我们的实验数据是原始皮肤反射率（采样远高于脉搏率频率），我们的目标是合奏PPG信号。基于摄像机的PPG采集和DRS的信号处理要求的细微差别如下所述。

基于摄像头的视频记录。通过对使用定义的sRoI和AC/DC标准化（即，除以其缓慢变化的分量，该缓慢变化的分量是通过使用截止频率为~40 bpm的Butterworth滤波器进行低通滤波而获得的）。反射模式PPG信号的幅度通常较低（特别是在红色波长中），但其信噪比（SNR）可以通过自适应带通滤波（ABPF）来改善。ABPF包括滤除信号中不是脉搏率频率基频倍数的频率分量。

ABPF应用在一个加和的方式（步长，256个样本;重叠因子，50%）与汉宁窗口。我们选择了脉率频率的基波和6次谐波以及每个中心频率周围一个bin的容差带。当可用时，用于识别收缩峰值和瞬时脉搏率的参考信号是手指脉搏血氧饱和度信号（与视频记录同步采集）。或者，参考是在绿色波长探测的PPG信号，因为这些具有最佳可用SNR。在ABPF之后，流中的PPG周期被压缩成集合平均（EA）波形，分别用于每个相机通道和信号维度。EA依赖于平均过程和信号周期中的高斯噪声消除。在实践中，根据收缩期峰值（在参考信号中识别）的时间划分周期，进行时间配准，最后使用修剪平均值算子（离群值拒绝，10%）进行平均。每个超分辨EA波形浓缩至少100个连续周期。

DRS记录的处理。作为预处理步骤，DRS流需要针对加性传感器噪声进行校准。这是通过减去每个波长λ中的本底噪声来完成的。通过将原始反射率表示为DR(t, λ)，其校准表示为

$$DR(t, \lambda) = \frac{DR(t, \lambda) - DR_{REF}(t, \lambda)}{DR_{REF}(t, \lambda) - DR_{DARK}(\lambda)}, \quad (1)$$

其中DR(λ)表示完全黑暗中的噪声水平。类似地，DR(λ)表示参考标准（型号WS-1，从250-1500 nm反射率>98%，Ocean Optics, Inc.）DR记录被处理以获得反射PPG-振幅和PPG-相位谱。

皮肤反射率和远程PPG的蒙特卡罗模拟。用蒙特卡罗方法模拟了远程PPG的频谱和深度源。Huelsbusch 在此之前进行了这些努力，但他假设远程PPG信号完全来自毛细血管环路，以及他高估的血液浓度和皮肤散射系数，导致红IR中PPG信号的低估。我们使用DRS文献和/或基于我们的实验估计的参数克服了这些问题。我们模拟了在一组组织特征下，舒张和收缩状态下光子通过组织的迁移，包括SpO和组织中的血液浓度，其中收缩状态通过动脉血液在舒张状态上的增量增加来获得。在450 - 1000 nm范围内的多个皮肤层上计算数据。

我们使用公开可用的GPU-MCML代码包，该代码包能够模拟光子在具有可调空间维度和分辨率的多层混浊介质中的传播。场景的几何形状在圆柱坐标系中指定，其中发射器以原点为中心并垂直于组织表面。发射器配置近似于来自无限窄光束的准直光。MCML的输入 (.mci) 文件包括皮肤结构参数、吸收和散射系数以及生理参数（如SpO、血液浓度、黑色素含量等）。为参考和压缩皮肤实施了单独的模型。

| Skin layers | <i>n</i> | <i>d_l</i> (cm) | <i>C_b</i> | <i>C_w</i> | <i>v_d</i> (μm) |
|-------------|----------|---------------------------|----------------------|----------------------|--|
| 1-EPI | 1.33 | 0.08 | 0 | 0.20 | 0 |
| 2-CL | 1.37 | 0.015 | 0.004 | 0.65 | 10 |
| 3-UP | 1.40 | 0.008 | 0.02 | 0.65 | 20 |
| 4-RD | 1.40 | 0.12 | 0.004 | 0.65 | 20 |
| 5-DP | 1.40 | 0.05 | 0.04 | 0.65 | 40 |
| 6-SC | 1.44 | 0.5 | 0.03 | 0.05 | 50 |

Table 1. Layer settings for normal/reference skin.

| Skin layers | <i>n</i> | <i>d_l</i> (cm) | <i>C_b</i> | <i>C_w</i> | <i>v_d</i> (μm) |
|-------------|----------|---------------------------|----------------------|----------------------|--|
| 1-EPI | 1.33 | 0.08 | 0 | 0.05 | 0 |
| 2-CL | 1.37 | 0.008 | 0.0012 | 0.15 | 10 |
| 3-UP | 1.40 | 0.004 | 0.0024 | 0.15 | 20 |
| 4-RD & DP | 1.40 | 0.1 | 0.024 | 0.15 | 20 |
| 5-SC | 1.44 | 0.2 | 0.036 | 0.35 | 40 |

Table 2. Layer settings for compressed skin.

Tissue Model. Figure 2 illustrates a multilayered model of normal glabrous (non hairy) skin tissue. The model consists of six homogeneous layers with different fractions of water, C_w , blood, C_b , and fat, C_f . Table 1 lists layer thicknesses, water and blood fractions for each skin layer—numbered from 1 to 6 (deepest)—in the diastolic state. The first layer listed is the epidermis. At the palm or finger pad, its thickness is high in comparison with other skin sites⁴⁶. The palm also features a fivefold lower density of melanocytes than at other skin areas⁴⁷. Accordingly, melanin was not included in our model. For the remaining layers, the optical and anatomical properties of our skin geometry are similar to previous work^{21,23,48}, though the average blood concentration in the dermis, C_b , is lower. This setting conforms with recent DRS studies^{42,49} indicating that C_b is within 1–3%.

The refractive index for all internal surface interfaces increases gradually from 1.33 at the surface to 1.44 at the bottom interface. The arterio-venous ratio ($r_a:r_v$) corresponds to the diastolic state and was applied to all dermal layers in the diastolic state⁵⁰. For the reference condition, $r_a:r_v$ was set at 50%:50%. Additional settings are as follows: the arterial oxygen saturation SpO_2 was set at 97% and the venous oxygen saturation, SvO_2 , was set 30% lower; and the fat concentration, C_f was set at 40% at the subcutis⁴². The vessel diameters per dermal layer, v_d , were estimated from the literature⁵¹.

Table 2 lists the adaptations made to mimic the skin compression status. In short, the dermal water and blood volume concentrations reduced, whereas pooling of blood (mostly venous) was implemented at the subcutis. The $r_a:r_v$ ratio was set at 100%:0 at the dermal layers and 75%:25% at the SC.

Absorption settings. The absorption coefficients of the skin layers were set differently for the epidermis and for the dermal layers. The epidermal absorption coefficient, $\mu_{a,EPI}$, was estimated as a combination of background tissue, $\mu_{a,base,EPI}$, and water:

$$\mu_{a,EPI}(\lambda) = C_w \mu_{a,water}(\lambda) + (1 - C_w) \mu_{a,base,EPI}(\lambda). \quad (2)$$

$\mu_{a,water}$ was determined from Palmer⁵² and Smith⁵³. The baseline tissue absorption for the epidermis, $\mu_{a,base,EPI}$, translates the effect of connective tissue and was implemented from Jacques³⁷:

$$\mu_{a,base,EPI}(\lambda) = \gamma \left[0.244 + 85.3 \exp\left(-\frac{\lambda - 154}{66.2}\right) \right]. \quad (3)$$

The wavelength, λ , is specified in nm and the factor $\gamma = 0.5$ accounts for water losses during *ex vivo* measurements. The absorption coefficient for the dermal layers and subcutis during diastole, $\mu_a^{(d)}(l, \lambda)$, $l \in \dots, 6$, were estimated as a sum of non-blood tissue absorption coefficient, $\mu_a^{(d)}(l, \lambda)$, and blood absorption, weighted by their respective concentrations within the layer. For convenience, the subscripts (l) and (λ) are omitted in the remainder of this section. $\mu_{a,nb}^{(d)}$ is set as follows:

$$\mu_{a,nb}^{(d)} = C_f \mu_{a,fat} + (1 - C_f) C_w \mu_{a,water} + (1 - C_f) (1 - C_w) \mu_{a,base}. \quad (4)$$

For the dermal background absorption, $\mu_{a,base}$, the exponential dependency of Eq. 3 was taken from Salomatina *et al.*⁵⁴:

$$\mu_{a,base} = \gamma \frac{C_w}{C_{w0}} \left[0.244 + 16.82 \exp\left(-\frac{\lambda - 400}{80.5}\right) \right] \quad (5)$$

| 皮肤层 | n | d (cm) | C_w | C_f | v (μm) |
|--------|------|----------|-------|-------|-----------------------|
| 1-肾上腺素 | 1.33 | 0.08 | 0 | 0.20 | 0 |
| 2-CL | 1.37 | 0.015 | 0.004 | 0.65 | 10 |
| 3-UP | 1.40 | 0.008 | 0.02 | 0.65 | 20 |
| 4-RD | 1.40 | 0.12 | 0.004 | 0.65 | 20 |
| 5-DP | 1.40 | 0.05 | 0.04 | 0.65 | 40 |
| 6-SC | 1.44 | 0.5 | 0.03 | 0.05 | 50 |

表1.正常/参考蒙皮的层设置。

| 表层 | n | d (cm) | C_w | C_f | v (μm) |
|---------|------|----------|--------|-------|-----------------------|
| 1-肾上腺素 | 1.33 | 0.08 | 0 | 0.05 | 0 |
| 2-CL | 1.37 | 0.008 | 0.0012 | 0.15 | 10 |
| 3-UP | 1.40 | 0.004 | 0.0024 | 0.15 | 20 |
| 4-研发与发展 | 1.40 | 0.1 | 0.024 | 0.15 | 20 |
| 5-SC | 1.44 | 0.2 | 0.036 | 0.35 | 40 |

表2.压缩皮肤的层设置。

组织模型。图2示出了正常无毛（无毛）皮肤组织的多层模型。该模型由六个均质层组成，具有不同的水（C_w）、血液（C_b）和脂肪（C_f）分数。表1列出了舒张状态下每个皮肤层的层厚度、水和血液分数-编号为1至6（最深）。列出的第一层是表皮。在手掌或指肚处，其厚度与其他皮肤部位相比较高。手掌的黑色素细胞密度也比其他皮肤区域低五倍。因此，黑色素不包括在我们的模型中。对于剩余的层，我们的皮肤几何形状的光学和解剖学特性与以前的工作相似，尽管真皮中的平均血液浓度C较低。该设置与最近的DRS研究一致，表明C在1-3%范围内。

所有内表面界面的折射率从表面处的1.33逐渐增加到底部界面处的1.44。动静脉比（r: r'）对应于舒张状态，并适用于舒张状态下的所有真皮层。对于参比条件，r: r'设定为50%: 50%。其他设置如下：动脉血氧饱和度SpO设置为97%，静脉血氧饱和度SvO设置为低30%;皮下组织的脂肪浓度C设置为40%。根据文献估计每个真皮层的血管直径v。

表2列出了为模拟皮肤压缩状态而进行的调整。简而言之，真皮水和血容量浓度降低，而血液（主要是静脉）汇集在皮下组织中。真皮层的r: r'比设定为100%: 0，SC的r: r'比设定为75%: 25%。

吸收设置。对于表皮和真皮层，皮肤层的吸收系数被设置为不同。表皮吸收系数μ_{ep}估计为背景组织μ和水的组合：

$$\mu_{\text{肾上腺素}}(\lambda) = C_w \mu_w + (1 - C_w) \mu_{\text{基础肾上腺素}}(\lambda). \quad (2)$$

μ由Palmer和Smith确定。表皮的基线组织吸收μ转化为结缔组织的影响，并由Jacques实施：

$$\mu_{\text{基础肾上腺素}}(\lambda) = \gamma \cdot 0.244 + 85.3 \exp \left(-\frac{\lambda - 154}{66.2} \right). \quad (3)$$

波长λ以nm为单位指定，因子γ=0.5说明了离体测量期间的水分损失。吸收过程中真皮层和皮下组织的吸收系数，μ_{ad}由脂肪液组织吸收系数的各自浓度加权。为方便起见，本节部分省略了下标（1）和（λ）。μ_i设置如下：

$$\mu_{a,fb}^{(i)} = C_f \mu_{fb} + (1 - C_f) C_w \mu_w + (1 - C_f)(1 - C_w) \mu_{ad}. \quad (4)$$

对于皮肤背景吸收，μ_{ad}方程的指数依赖性。3个从Salomatina et al.:

$$\mu_{ad} = \gamma \frac{C_w \cdot 0.244 + 16.82 \exp \left(-\frac{\lambda - 400}{80.5} \right)}{C_{w,0}} \downarrow \downarrow \downarrow \quad (5)$$

where γ was set as 0.5 for dermal layers ($l=2 \dots 5$) and 0.25 for the subcutis ($l=6$). The coefficient $C_{w0}=0.65$ accounts for the fact that background measurements of $\mu_{a,base}(l)$ are performed at about 65%. These settings are aimed at meeting the absorption coefficient measurements of the bloodless dermis and subcutis of Simpson *et al.*⁵⁵.

We account for the fact that a fraction of the incident light is reflected in the vessel walls, meaning that the *apparent* blood volume that interacts with light is lower than the actual blood concentration at the skin. This effect is called self-shielding and is in conflict with the assumption of homogeneous mixture between bloodless skin tissue and blood⁵⁶. A correcting factor for this effect is easily performed by setting a function, $f[.]$, that translates effective dermal blood concentration (Cb) *apparent* (Cb'). $f[.]$ is influenced by the product of the average vessel diameter and by the blood absorption of the layers, $\mu_a v_d$. For collimated light, $f[.]$ is an exponentially decaying function given by

$$f[\mu_a v_d] = \frac{1}{1 + 1.007(\mu_a v_d/2)^{1.228}}. \quad (6)$$

Self-shielding is negligible in the red-IR range since μ_a is very low; i.e., $f[\mu_a v_d] \approx 1$. For wavelengths at the 500–580 nm range, $f[\mu_a v_d]$ reaches about 0.7 at the LD and SC (where the vessel diameter is $\sim 40 \mu\text{m}$) but only about 0.85 at the upper dermis, which is where most blue-green photons interact with tissue. Thus, the discrete absorbers correction has a minor influence on the accuracy of PPG simulations, although we implemented it for the sake of completeness. Accordingly, the diastolic arterial and venous blood fractions, $f_a^{(d)}$ and $f_v^{(d)}$, and the $Cb'^{(d)}$ at pulsating layers were set as follows:

$$f_a^{(d)} = r_a \ Cb \ f[v_d \ ((1 - SpO_2)\mu_{a,Hb} + SpO_2\mu_{a,HbO_2})], \quad (7)$$

$$f_v^{(d)} = r_v \ Cb \ f[v_d \ ((1 - SvO_2)\mu_{a,Hb} + SvO_2\mu_{a,HbO_2})], \quad (8)$$

$$Cb'^{(d)} = f_a^{(d)} + f_v^{(d)}. \quad (9)$$

Using the absorbance spectra of deoxygenated and oxygenated hemoglobin, $\mu_{a,Hb}$ and μ_{a,HbO_2} , respectively, compiled by Bosschaart *et al.*⁵⁷, the diastolic absorption coefficient of the total tissue was given by

$$\begin{aligned} \mu_a^{(d)} &= f_a^{(d)} \ ((1 - SpO_2) \mu_{a,Hb} + SpO_2\mu_{a,HbO_2}) + \dots \\ f_v^{(d)} \ ((1 - SvO_2) \mu_{a,Hb} + SvO_2\mu_{a,HbO_2}) + Cb' \mu_{a,water} + (1 - Cb) \mu_{a,nb}^{(d)}. \end{aligned} \quad (10)$$

Systole is modeled as fractional pulsatile increases, p , of arterial blood in pulsating layers. The systolic $f_a^{(s)}$ and $Cb'^{(s)}$ are

$$f_a^{(s)} = f_a^{(d)} + p \ f[v_d \ ((1 - SpO_2)\mu_{a,Hb} + SpO_2\mu_{a,HbO_2})], \quad (11)$$

$$Cb'^{(s)} = Cb' + p \ f[v_d \ ((1 - SpO_2)\mu_{a,Hb} + SpO_2\mu_{a,HbO_2})]. \quad (12)$$

Two possible mechanisms ensure model consistency during the systolic increase of arterial blood volume. Either pulsatile changes are compensated by water displacements^{50,58} (WD) or there is layer expansion (LE) to accommodate the additional fluid; i.e., micro-modulations of layers thickness⁵⁹. In LE, the layers thickness during systole is set in proportion to p :

$$d^{(s)} = d \ (1 + Cb'^{(s)} \ p). \quad (13)$$

By defining the expansion factor for each layer, E , as $d/d^{(s)}$, the absorption coefficient during systole is

$$\begin{aligned} \mu_a^{(s)} &= E [f_a^{(s)} \ ((1 - SpO_2)\mu_{a,Hb} + SpO_2\mu_{a,HbO_2}) + \dots \\ f_v^{(s)} \ ((1 - SvO_2)\mu_{a,Hb} + SvO_2\mu_{a,HbO_2}) + Cb'^{(s)} \mu_{a,w} + (1 - Cb'^{(s)}) \mu_{a,nb}^{(d)}]. \end{aligned} \quad (14)$$

In practice, the simulations obtained under WS or LE are similar (see Fig. 9). This is unsurprising since the blood concentration at the dermis is only about 2–3% and E is close to unity. Accordingly, only LE was implemented.

Scattering settings. Skin scattering is conceptually regarded as a summation of Rayleigh and Mie scattering⁶⁰. In spite of fundamental differences, the diffuse light setting is well approximated by assuming that scattering losses occur in the depth dimension only, thus justifying that dermal scattering is reasonably described by a one-term expression, or even set as wavelength-independent²¹. We derived the reduced scattering coefficient for the dermal tissue, μ'_s , from the observations of Simpson and Shimada^{39,55}:

其中，对于真皮层， γ 设定为0.5 ($l = 2.5$)，对于皮下组织， γ 设定为0.25 ($l = 6$)。系数C = 0.65说明 μ (l) 的背景测量在约65%处进行。这些设置旨在满足Simpson等人的无血真皮和皮下组织的吸收系数测量。

我们解释了一部分入射光在血管壁中反射的事实，这意味着与光相互作用的表观血液体积低于皮肤处的实际血液浓度。这种效应被称为自屏蔽，并且与无血皮肤组织和血液之间的均匀混合物的假设相冲突。通过设置函数f [·]，其转化为有效皮肤血药浓度 (Cb) 表观 (Cb')。f [·]受平均血管直径和各层血液吸收的乘积 μv 的影响。对于准直光，f [·]是一个指数衰减函数，由下式给出：

$$f[\mu_{av}] = \frac{1}{1 + 1.007(\mu_{av}/2)^{1.228}}. \quad (6)$$

自屏蔽在红-IR范围内是可忽略的，因为 μ 非常低；即， $f[\mu v] \leq 1$ 。对于500-580 nm范围内的波长，f [μv]在LD和SC（血管直径约为40 μm ）处达到约0.7，但在上层真皮处仅为约0.85，这是大多数蓝绿色光子与组织相互作用的地方。因此，离散吸收体校正对PPG模拟的准确性影响很小，尽管我们为了完整性而实施了它。因此，舒张期动脉和静脉血液分数f和f'以及脉动层的Cb'设置如下：

$$f_a^{(d)} = r_a Cb f v_d \left((1 - SpO_2) \mu_{a,Hb} + SpO_2 \mu_{a,HbO_2} \right), \quad (7)$$

$$f_v^{(d)} = r_v Cb f v_d \left((1 - SvO_2) \mu_{v,Hb} + SvO_2 \mu_{v,HbO_2} \right), \quad (8)$$

$$Cb'^{(d)} = f_a^{(d)} + f_v^{(d)}. \quad (9)$$

利用脱氧血红蛋白和氧合血红蛋白的吸收光谱，₁，₂， 分别，由Bosschaart等人编制，总组织的舒张期吸收系数由下式给出：

$$\begin{aligned} \mu_a^{(d)} &= f_a^{(d)} \left((1 - SpO_2) \mu_{a,Hb} + SpO_2 \mu_{a,HbO_2} \right) + \dots \\ f_v^{(d)} &= \left((1 - SvO_2) \mu_{v,Hb} + SvO_2 \mu_{v,HbO_2} \right) + Cb' \mu_w + (1 - Cb) \mu_{anb}^{(d)}. \end{aligned} \quad (10)$$

收缩期被建模为脉动层中动脉血的脉动增加分数p。收缩期f和Cb' 为

$$f_a^{(s)} = f_a^{(d)} + p f v_d \left((1 - SpO_2) \mu_{a,Hb} + SpO_2 \mu_{a,HbO_2} \right), \quad (11)$$

$$Cb'^{(s)} = Cb' + p f v_d \left((1 - SpO_2) \mu_{a,Hb} + SpO_2 \mu_{a,HbO_2} \right). \quad (12)$$

两种可能的机制确保了动脉血容量收缩期增加期间模型的一致性。脉动变化通过水置换 (WD) 补偿，或者存在层膨胀 (LE) 以容纳额外的流体；即，层厚度的微调。在LE中，收缩期间的层厚度与p成比例地设置：

$$d^{(s)} = d (1 + Cb'^{(s)} p). \quad (13)$$

通过将每层的膨胀因子E定义为d/d，收缩期间的吸收系数为：

$$\begin{aligned} \mu_a^{(s)} &= E f_a^{(s)} \left((1 - SpO_2) \mu_{a,Hb} + SpO_2 \mu_{a,HbO_2} \right) + \dots \\ f_v^{(s)} &= \left((1 - SvO_2) \mu_{v,Hb} + SvO_2 \mu_{v,HbO_2} \right) + Cb'^{(s)} \mu_{aw} + (1 - Cb) \mu_{anb}^{(d)}. \end{aligned} \quad (14)$$

在实践中，WS或LE下获得的模拟是相似的（见图9）。这并不令人惊讶，因为真皮处的血液浓度仅为约2-3%，并且E接近于1。因此，仅执行LE。

分散设置。皮肤散射在概念上被认为是瑞利散射和米氏散射的总和。尽管存在根本差异，但通过假设散射损失仅发生在深度维度上，漫射光设置可以很好地近似，从而证明皮肤散射可以通过一项表达式合理描述，甚至可以设置为与波长无关。我们从Simpson和Shimada的观察中推导出皮肤组织的约化散射系数 μ' ：

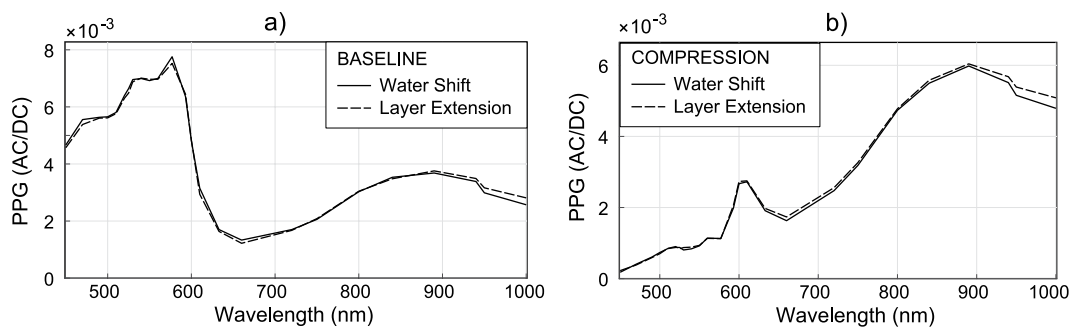


Figure 9. The similarity of simulation outcomes with WS and LE on (a) normal and (b) compressed skin models.

$$\mu'_s = c_0(l, \lambda) \lambda^{-b}, \quad (15)$$

where $c_0(l, \lambda)$ is a calibration constant that sets the reduced scattering μ'_s to (EPI: 15 cm^{-1} ; CL, UD, RD, LD: 20 cm^{-1} ; SC: 10 cm^{-1})⁵⁵. The decaying factor b was estimated as 0.1 below 580 nm and 0.05 otherwise. Similar to Simpson *et al.*⁵⁵, the anisotropy factor was assumed to be 0.9 for tissue.

Simulating remote PPG. For each simulated wavelength, $\lambda \in <450, 1000> \text{ nm}$, and skin layer, $l = 1 \dots 6$, the relevant outputs from MCML for expressing the simulated remote PPG spectra are the fraction of photons reaching the surface per cm as a function of radial distance from the origin, $Rdr(r, \lambda, l)$, and the total diffuse reflectance, $Rdt(\lambda, l)$, expressed as fraction of total emitted photons.

Matlab was used for further processing. The diastolic-systolic diffuse reflectance outputs were applied to mimic the PPG spectra for remote and for contact-based acquisition. The remote normalized pulsatile reflectance PPG, PPG_{REM} , was AC/DC normalized for pulsating layer, l , as normalized fractions of the total incident photons; i.e.,

$$PPG_{REM}(\lambda, l) = \frac{RdT^d(\lambda, l) - RdT^s(\lambda, l)}{RdT^d(\lambda, l)}. \quad (16)$$

where RdT^s , and RdT^d denote the total diffuse reflectance during systole and diastole, respectively. Since each wavelength needs to be simulated under diastolic and systolic conditions, for a skin model with five pulsating layers at least six simulation runs were required, per wavelength. Each simulation run consisted of 10E8 to 40E8 photons and required approximately 10 min of processing time on a Linux server operating an NVIDIA GeForce GTX TITAN with compute capability 3.5 (14 SMs).

Optical penetration depth and depth-origin of PPG. The Matlab routines *lookmcml.m* and *getmcml.m* (publicly available at <http://omlc.org/software/mc/>) were used to compute the optical fluxes as a function of the skin depth from the MCML simulation output files. Care was taken to remove spurious peaks in the skin layer boundaries, thus ensuring that the flux functions are continuous along the depth axis.

For each wavelength and skin configuration, a flux function was computed for the diastolic state, $F^{(d)}(z)$, allowing us to express the optical penetration depth of the incident light as the skin depth, oriented along the z-axis, that is reached by $1 - \frac{1}{e}$ of the incident photons. Mathematically, the PD was obtained by solving the following equation:

$$\frac{\sum_{z=0}^{PD} F^{(d)}(PD)}{\sum_{z=0}^{T_s} F^{(d)}(z)} = 1 - \frac{1}{e} \approx 63.2\%, \quad (17)$$

where T_s is the total tissue thickness. The depth-origin (DO) of the PPG signals was computed based on the flux perturbations induced during systole for each pulsatile skin layer. By weighting these according to the relative proportions of pulsatile strength in the various modeled layers, w_l , the differential flow due to BVs is given by

$$\Delta F(z) = \sum_l (F^{(d)}(z) - F_l^{(s)}(z)) w_l^T, \quad (18)$$

where $F_l^{(s)}$ denotes the flux perturbed during systole in layer l . Lastly, the DO of the PPG signal was determined as the depth for which the cumulative sum of ΔF is $1 - \frac{1}{e}$; i.e.,

$$\frac{\sum_{z=0}^{DO} \Delta F(DO)}{\sum_{z=0}^{T_s} \Delta F(z)} = 1 - \frac{1}{e}. \quad (19)$$

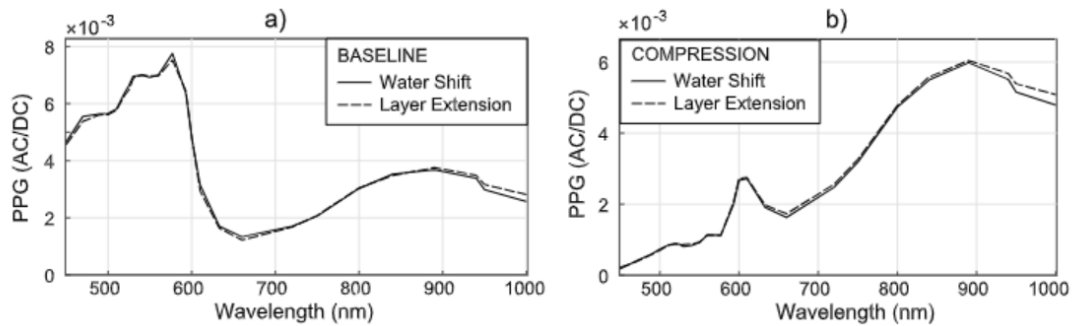


图9. WS和LE在(a)正常和(B)压缩皮肤模型上模拟结果的相似性。

$$\mu'_s = G_1(\lambda) \lambda^b, \quad (15)$$

其中 $c(l, \lambda)$ 是将约化散射 μ' 设置为 (EPI: 15 cm; CL, UD, RD, LD: 20 cm; SC: 10 cm) 的校准常数。衰减因子 B 在 580 nm 以下估计为 0.1, 否则估计为 0.05。与 Simpson 等人相似, 假设组织的各向异性因子为 0.9。

模拟远程PPG。对于每个模拟的波长 $\lambda \in [450, 1000]$ nm 和皮肤层 $l = 1.6$, 来自MCML的用于表达模拟的远程 PPG 光谱的相关输出是作为距原点的径向距离的函数的每cm到达表面的光子的分数 $Rdr(r, \lambda, l)$, 以及表示为总发射光子的分数的总漫反射率 $Rdt(\lambda, l)$ 。

Matlab was used for further processing. The diastolic-systolic diffuse reflectance outputs were applied to mimic the PPG spectra for remote and for contact-based acquisition. The remote normalized pulsatile reflectance PPG, PPG, was

AC/DC normalized for pulsating layer, l , as normalized fractions of the total incident photons; i.e., ?

$$PPG_{REM}(\lambda)l = \frac{RDT(\lambda)Rdr(\lambda, l)}{RdT(\lambda)l}. \quad (16)$$

其中 RdT 和 Rdr 分别表示收缩期和舒张期的总漫反射率。由于每个波长需要在舒张和收缩条件下进行模拟, 因此对于具有五个脉动层的皮肤模型, 每个波长至少需要六次模拟运行。每次模拟运行由 10 E8 到 40 E8 个光子组成, 并且在运行具有计算能力 3.5 (14 SM) 的 NVIDIA GeForce GTX TITAN 的 Linux 服务器上需要大约 10 分钟的处理时间。

光学穿透深度和 PPG 的深度原点。使用 Matlab 例程 lookmcml.m 和 getmcml.m (可在 <http://omlc.org/software/mc/> 上公开获得) 从 MCML 模拟输出文件计算作为趋肤深度的函数的光通量。注意去除表层边界中的伪峰, 从而确保通量函数沿深度轴沿着是连续的。

对于每个波长和皮肤配置, 计算舒张状态的通量函数 $F(z)$, 允许我们将入射光的光学穿透深度表示为趋肤深度, 其沿着 z 轴取向, 通过 -

1 \int_e^1 入射的光子。在数学上, 通过求解以下方程获得 PD:

$$\frac{\sum_{z=0}^{PD} F(z)}{\sum_{z=0}^{T_s} F(z)} = 1 - \frac{1}{e} \approx 63.2\%, \quad (17)$$

其中 T_s 是总组织厚度。PPG 信号的深度原点 (DO) 是基于每个脉动皮肤层在收缩期间引起的通量扰动来计算的。通过根据不同建模层中脉动强度的相对比例 w_l 对这些进行加权, 由 BVV 引起的差异流量由下式给出:

$$\Delta F(z) = \sum_l (F(z) - F_l(z)) w_l, \quad (18)$$

其中 F 表示在层 l 中的收缩期间扰动的通量。最后, PPG 信号的 DO 被确定为 ΔF 的累积和为 -0.001 的深度。

$1 - \frac{1}{e}; y,$

$$\frac{\sum_{z=0}^{DO} \Delta F(z)}{\sum_{z=0}^{T_s} \Delta F(z)} = 1 - \frac{1}{e}. \quad (19)$$

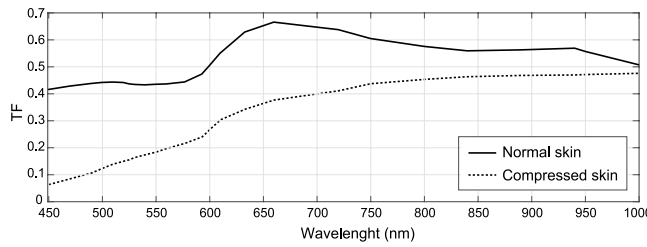


Figure 10. TF functions for converting reflection-mode to remote PPG spectra. These describe the “distortion” effect introduced by the OFP’s ferrule on the PPG spectrum and evidence the boosting of, mostly, PPG-amplitudes <600 nm.

Indirect measurements of the remote PPG spectra by using transfer functions. Since the used OFP is shielded by a ferrule (which clips shallow photon paths) a correction is needed if the reflection-PPG spectra, PPG_{OFP} , are to be used for drawing considerations to the remote setting. In this investigation, the [pseudo] remote PPG-amplitude spectrum, PPG_{REM} , is estimated from PPG_{OFP} based on a transfer function such that $TF = PPG_{REM}/PPG_{OFP}$. The numerical estimation of such TF began with simulating, in MCML, the remote diffuse reflectance (DR) in the 450–1000 nm. The uncalibrated remote DR from the skin, during systole and diastole, were obtained as functions of the source distance. Those were integrated from $Rd_r(n_r, \lambda)$ as

$$uDR^d(i, \lambda) = \sum_{n_r=i}^{R=3000} Rd_r^d(n_r, \lambda), \quad (20)$$

$$uDR^s(i, \lambda) = \sum_{n_r=i}^{R=3000} Rd_r^s(n_r, \lambda), \quad (21)$$

where the index n_r refers to source distance. For a radial resolution of 0.0005 cm and 3000 grid points, the spanned radius ranges up to 1.5 cm. The correction factors for diastolic and systolic DR, $C^d(\lambda)$ and $C^s(\lambda)$, are obtained as

$$C^d(\lambda) = RdT^d(\lambda)/uDR^d(n_e, \lambda), \quad (22)$$

$$C^s(\lambda) = RdT^s(\lambda)/uDR^s(n_e, \lambda). \quad (23)$$

with n_e set to 10 to prevent numerical inaccuracies. The calibrated DR for systole and diastole becomes

$$DR_{OFP}^{(s)}(\lambda) = C^{(s)}(\lambda) uDR^{(s)}(n_{r0}, \lambda), \quad (24)$$

$$DR_{OFP}^{(d)}(\lambda) = C^{(d)}(\lambda) uDR^{(d)}(n_{r0}, \lambda). \quad (25)$$

with $n_{r0}=278$. Finally, the reflectance PPG signal the OFP and layer l was obtained as

$$PPG_{OFP}(l, \lambda) = \frac{DR_{OFP}^{(d)}(\lambda) - DR_{OFP}^{(s)}(\lambda)}{DR_{OFP}^{(d)}(\lambda)}. \quad (26)$$

The TF from reflectance to [pseudo] remote-PPG was finally given by

$$TF(n_{r0}, \lambda) = \frac{\sum_l PPG_{REM}(l, \lambda) w_l}{\sum_l PPG_{OFP}(l, n_{r0}, \lambda) w_l}. \quad (27)$$

The compression curves for normal and compressed skin are shown in Fig. 10. Both indicate that the OFP configuration boosts the PPG-amplitude, particularly in blue-green wavelengths.

Simulation precision. The average simulation errors for the remote PPG spectra—expressed as standard deviations over the means—is 4.7% for the 475–1000 nm range. This error estimate was based on four repeated runs of the compressed skin model.

References

- Allen, J. Photoplethysmography and its application in clinical physiological measurements. *Physiol. Meas.* **28**, 1–40 (2007).
- Verkruyse, W., Svaasand, L. O. & Nelson, J. S. Remote plethysmographic imaging using ambient light. *Opt. Express* **16**, 21434–21445 (2008).
- Wukitsch, M. W., Petterson, M. T., Tobler, D. R. & Pologe, J. A. Pulse oximetry: analysis of theory, technology, and practice. *J Clin Monit* **4**, 290–301 (1988).
- Rouast, P. V., Adam, M. T., Chuiong, R., Cornforth, D. & Lux, E. Remote heart rate measurement using low-cost RGB face video: a technical literature review. *Front. Comput. Sci.* 1–17 (2016).

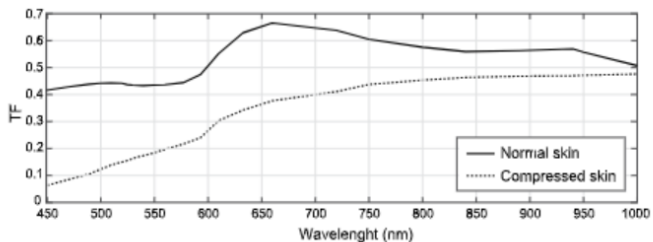


图10.用于将反射模式转换为远程PPG光谱的TF功能。这些描述了由OFP的套圈对PPG光谱引入的“失真”效应，并且证明了大多数PPG振幅<600 nm的增强。

通过使用传递函数间接测量远程PPG光谱。由于所使用的OFP被套圈（其夹持浅光子路径）屏蔽，因此如果反射PPG光谱PPG将用于远程设置的绘图考虑，则需要进行校正。在该研究中，基于传递函数从PPG估计[伪]远程PPG幅度谱PPG，使得 $TF = PPG_REM / PPG$ 。这种TF的数值估计开始于在MCML中模拟450–1000 nm的远程漫反射(DR)。在心脏收缩期和心脏舒张期，从皮肤获得的未校准的远程DR作为源距离的函数。这些从 $Rd(n, \lambda)$ 积分分为

$$uDR^d(i, \lambda) = \sum_{n_r=i}^{R=3000} Rd_r^d(n_r, \lambda), \quad (20)$$

$$uDR^s(i, \lambda) = \sum_{n_r=i}^{R=3000} Rd_r^s(n_r, \lambda), \quad (21)$$

其中指数n表示源距离。对于0.0005 cm的径向分辨率和3000个网格点，跨度半径范围可达1.5 cm。舒张期和收缩期DR的校正因子 $C(\lambda)$ 和 $C_s(\lambda)$ 如下所示：

$$C^d(\lambda) = RdT^d(\lambda) / uDR^d(n_s, \lambda), \quad (22)$$

$$C^s(\lambda) = RdT^s(\lambda) / uDR^s(n_s, \lambda), \quad (23)$$

其中n设置为10以防止数值不准确。收缩期和舒张末期的校准DR变为

$$DR_{OFP}^{(d)}(\lambda) = C^d(\lambda) uDR^d(n_{r0}, \lambda), \quad (24)$$

$$DR_{OFP}^{(s)}(\lambda) = C^s(\lambda) uDR^s(n_{r0}, \lambda), \quad (25)$$

$n = 278$ 最后，OFP和层1的反射PPG信号被获得为：

$$PPG_{OFP}(l, \lambda) = \frac{DR_{OFP}^{(d)}(\lambda) - \lambda DR_{OFP}^{(s)}(\lambda)}{DR_{OFP}^{(d)}(\lambda)}. \quad (26)$$

从反射率到[伪]远程PPG的TF最终由下式给出：

$$TF(n_{r0}, \lambda) = \frac{\sum_l PPG_{REM}(l) \lambda w_l}{\sum_l PPG_{OFP}(l, n_{r0}, \lambda) w_l}. \quad (27)$$

正常和受压皮肤的压缩曲线如图10所示。两者都表明OFP配置增强PPG振幅，特别是在蓝绿色波长中。

模拟精度。对于475–1000 nm范围，远程PPG光谱的平均模拟误差（表示为平均值的标准差）为4.7%。该误差估计基于压缩皮肤模型的四次重复运行。

参考文献

1. 艾伦, J.光电体积描记法及其在临床生理测量中的应用。生理学测量28, 1-40 (2007)。
2. Verkruyse, W., 斯瓦桑德湖O. & 纳尔逊, J.S.使用环境光的远程体积描记成像。Opt. Express 16, 21434-21445 (2008)。
3. Wukitsch, M. W., Petterson, M. T., Tobler, D. R. & Pologe, J. A.脉搏血氧饱和度：理论、技术与实践分析。临床监测杂志4, 290-301 (1988)。
4. Rouast, P. V., Adam, M. T., Chuiiong Cornforth, D. & Lux, E.使用低成本RGB人脸视频进行远程心率测量：技术文献综述。前面Comput. Sci. 1-17 (2016)。

5. Verkruyse, W. *et al.* Calibration of contactless pulse oximetry. *Anesth. Analg* **124**, 136–145 (2016).
6. Amelard, R. *et al.* Feasibility of long-distance heart rate monitoring using transmittance photoplethysmographic imaging (ppgi). *Scientific Reports* **5**, 14637 (2015).
7. de Haan, G. & Jeanne, V. Robust pulse-rate from chrominance-based rPPG. *IEEE Transactions on Biomedical Engineering* **60**, 2878–2886 (2014).
8. van Gastel, M., Stuijk, S. & de Haan, G. New principle for measuring arterial blood oxygenation, enabling motion-robust remote monitoring. *Sci. Rep.* **6**, 38609 (2016).
9. Allen, J. & Howell, K. Microvascular imaging: techniques and opportunities for clinical physiol. meas. *Physiol. Meas.* **35**, 91–141 (2014).
10. Thatcher, J. E. *et al.* Multispectral and photoplethysmography optical imaging techniques identify important tissue characteristics in an animal model of tangential burn excision. *Journal of Burn Care & Research* **37**, 38–52 (2016).
11. Damianou, D. *The wavelength dependence of the photoplethysmogram and its implication to pulse oximetry*. Phd thesis, University of Nottingham, Department of Electrical and Electronic Engineering (1995).
12. Naslund, J., Pettersson, J., Lundeberg, T., Linnarsson, D. & Lindberg, L. G. Non-invasive continuous estimation of blood flow changes in human patellar bone. *Med Biol Eng Comput* **44**, 501–509 (2006).
13. Lindberg, L.-G., Sveider, P. & Oberg, P. A. Optical properties of blood in motion. In *OE/LASE 92*, vol. **32**, 116–122 (SPIE) (1993).
14. Shvartsman, L. D. & Fine, I. Optical transmission of blood: effect of erythrocyte aggregation. *IEEE Trans Biomed Eng* **50**, 1026–1033 (2003).
15. Kamshilin, A. A. *et al.* A new look at the essence of the imaging photoplethysmography. *Sci. Rep.* **5**, 10494 (2015).
16. Kamshilin, A. A., Miridonov, S., Teplov, V., Saarenheimo, R. & Nippolainen, E. Photoplethysmographic imaging of high spatial resolution. *Biomed. Opt. Express* **2**, 996–1006 (2011).
17. Moco, A., Stuijk, S. & de Haan, G. Ballistocardiographic artifacts in PPG imaging. *IEEE Trans Biomed Eng* **63**, 1804–1811 (2016).
18. Moco, A., Stuijk, S. & de Haan, G. Motion robust PPG-imaging through color channel mapping. *Biomed. Opt. Express* **7**, 1737–1754 (2016).
19. Anderson, R. R. & Parrish, J. A. The optics of human skin. *J Invest Dermatol* **77**, 13–19 (1981).
20. Agache, P. *Skin Structural Components: Physiology and Metrology*, 17–399 (Springer-Verlag, Berlin, 2014).
21. Meglinski, I. V. & Matcher, S. J. Computer simulation of the skin reflectance spectra. *Computer Methods and Programs in Biomedicine* **70**, 179–186 (2003).
22. Reuss, J. L. Multilayer modeling of reflectance pulse oximetry. *IEEE Trans. Biom. Eng.* **52**, 153–159 (2005).
23. Huelsbusch, M. An image-based functional method for opto-electronic detection of skin-perfusion. Phd thesis, RWTH Aachen dept. of EE. (in German) (2008).
24. Bergstrand, S., Lindberg, L. G., Ek, A. C., Linden, M. & Lindgren, M. Blood flow measurements at different depths using photoplethysmography and laser Doppler techniques. *Skin. Res. Technol.* **15**, 139–147 (2009).
25. Raamat, R., Jagomägi, K. & Talts, J. Calibrated photoplethysmographic estimation of digital pulse volume and arterial compliance. *Clinical Physiology and Functional Imaging* **27**, 354–362 (2007).
26. Baran, U., Choi, W. J. & Wang, R. K. Potential use of oct-based microangiography in clinical dermatology. *Skin Research and Technology* **22**, 238–246 (2016).
27. Mugit, N. *et al.* Association between nail-fold capillary findings and disease activity in dermatomyositis. *Rheumatology* **50**, 1091–1098 (2011).
28. Baran, U., Shi, L. & Wang, R. K. Capillary blood flow imaging within human finger cuticle using optical microangiography. *J. biophotonics* **8**, 46–51 (2015).
29. Secomb, T. W., Hsu, R. & Pries, A. R. Motion of red blood cells in a capillary with an endothelial surface layer: effect of flow velocity. *Am J Physiol Heart Circ Physiol* **281**, 629–636 (2001).
30. Volkov, M. V. *et al.* Video capillaroscopy clarifies mechanism of the photoplethysmographic waveform appearance. *Scientific Reports* **7**, 13298 (2017).
31. Mahler, F., Muheim, M. H., Intaglietta, M., Bollinger, A. & Anliker, M. Blood pressure fluctuations in human nailfold capillaries. *American Journal of Physiology-Heart and Circulatory Physiology* **236**, 888–893 (1979).
32. Hickey, M., Phillips, J. P. & Kyriacou, P. A. The effect of vascular changes on the photoplethysmographic signal at different hand elevations. *Physiol. Meas.* **36**, 425–440 (2015).
33. Jacques, S. L. & Wang, L. *Monte Carlo Modeling of Light Transport in Tissues*, 73–100 (Springer US, Boston, MA, 1995).
34. Wong, R., Geyer, S., Weninger, W., Guimberneau, J.-C. & Wong, J. K. The dynamic anatomy and patterning of skin. *Experimental Dermatology* 92–98 (2015).
35. Geyer, S. H., Nöhammer, M. M., Tinhofer, I. E. & Weninger, W. J. The dermal arteries of the human thumb pad. *Journal of Anatomy* **223**, 603–609 (2013).
36. Bashkatov, A. N., Genina, E. A. & Tuchin, V. V. Optical properties of skin, subcutaneous, and muscle tissues: A review. *Journal of Innovative Optical Health Sciences* **04**, 9–38 (2011).
37. Jacques, S. L. Optical properties of biological tissues: a review. *Phys Med Biol* **58**, 37–61 (2013).
38. Zonios, G. & Dimou, A. Light scattering spectroscopy of human skin *in vivo*. *Optics Express* **17**, 1256–1267 (2009).
39. Shimada, M., Yamada, Y., Itoh, M. & Yatagai, T. Melanin and blood concentration in a human skin model studied by multiple regression analysis: assessment by monte carlo simulation. *Phys Med Biol* **46**, 2397–406 (2001).
40. Delgado Atencio, J. A. *et al.* Influence of probe pressure on human skin diffuse reflectance spectroscopy measurements. *Optical Memory and Neural Networks* **18**, 6–14 (2009).
41. Reif, R. *et al.* Analysis of changes in reflectance measurements on biological tissues subjected to different probe pressures. *Journal of Biomedical Optics* **13**, 010502–010502–3 (2008).
42. Bjorgan, A., Milanic, M. & Randeberg, L. L. Estimation of skin optical parameters for real-time hyperspectral imaging applications. *Journal of Biomedical Optics* **19**, 066003–066003 (2014).
43. Corral, L. F., Paez, G. & Strojnik, M. Optimal wavelength selection for non-contact reflection photoplethysmography. In *Proc. SPIE*, vol. 8011, 801191–801191–7 (2011).
44. Blackford, E. B., Estepp, J. R. & McDuff, D. J. Remote spectral measurements of the blood volume pulse with applications for imaging photoplethysmography. In *SPIE BiOS*, vol. 10501, 8 (SPIE) (2018).
45. Alerstam, E. *et al.* Next-generation acceleration and code optimization for light transport in turbid media using gpus. *Biomedical Optics Express* **1**, 658–675 (2010).
46. Verma, G. *Fundamentals of Histology* (New Age International (P) Limited, Publishers, 2001).
47. Yamaguchi, Y. & Hearing, V. J. Melanocytes and their diseases. *Cold Spring Harb Perspect Med* **4**, a017046 (2014).
48. Tuchin, V. V. *et al.* Finger tissue model and blood perfused skin tissue phantom. In *Proc. SPIE*, vol. 7898, 78980–78980–11 (2011).
49. Yudovsky, D. & Pilon, L. Retrieving skin properties from *in vivo* spectral reflectance measurements. *J Biophotonics* **4**, 305–314 (2011).
50. Schmitt, J. M., Zhou, G. X., Walker, E. C. & Wall, R. T. Multilayer model of photon diffusion in skin. *J. Opt. Soc. Am. A* **7**, 2141–2153 (1990).
51. Braverman, I. M. *Anatomy and physiology of cutaneous microcirculation*, book section 1, 3–22 (CRC Press, Boca Raton, Florida, 1995).

5. Verkruyse, W. 等人, Calibration of incontacted pulse oximetry. 麻醉Analg 124, 136-145 (2016) .
6. 阿梅拉尔河等人, 使用透射式光电容积描记成像 (ppgi) 进行长距离心率监测的可行性。科学报告5, 14637 (2015) 。
7. de哈安、G. & Jeanne, V. 基于色度的rPPG的稳健脉搏率。IEEE Transactions on Biomedical Engineering 60, 2878-2886 (2014) 。
8. 货车Gastel, M., 斯图伊克, S. & de哈安, G. 测量动脉血氧的新原理, 实现运动稳健的远程监测。Sci. Rep. 6, 38609 (2016) 中描述的。
9. 艾伦, J.&豪厄尔, K. 微血管成像: 临床生理测量的技术和机会。生理学测量35, 91-141 (2014) 。
10. 撒切尔, J.E. 多光谱和光电体积描记光学成像技术在切线烧伤切除的动物模型中识别重要的组织特征。烧伤护理与研究杂志37, 38-52 (2016) 。
11. Damianou, D. 光电容积描记图的波长依赖性及其对脉搏血氧饱和度的意义。诺丁汉大学博士论文。电气和电子工程系 (1995年) 。
12. Naslund, J., Pettersson, J., Lundeberg, T., Linnarsson, D. & Lindberg, L. G. 人髌骨血流变化的无创连续估计。Med Biol Eng Comput 44, 501-509 (2006) .
13. 林德伯格湖G., Sveidler, P. & Oberg, P. A. 运动中血液的光学特性。在OE/LASE 92, 第32卷, 116-122 (SPIE) (1993) 中。
14. 什瓦茨曼湖D. 好吧, 我。血液的光透射: 红细胞聚集的影响。IEEE Trans Biomed Eng 50, 1026-1033 (2003) 。
15. Kamshilin, A. a. 等。对成像光电容积描记术本质的新认识。sci. Rep. 5, 10494 (2015) 中描述的。
16. Kamshilin, A.一、Miridonov, S., Teplov, V., 萨伦黑莫河& Nippolainen, E. 高空间分辨率的光电体积描记成像。BioMed. Opt. Express 2, 996 - 1006 (2011) 。
17. Moco, A., 斯图伊克, S. & de哈安, G. PPG成像中的心冲击描记伪影。IEEE Trans Biomed Eng 63, 1804-1811 (2016) 。
18. Moco, A., 斯图伊克, S. & de哈安, G. 通过颜色通道映射实现运动鲁棒PPG成像。BioMed. Opt. Express 7, 1737-1754 (2016) 。
19. 安德森河R. & Parrish, J. A. 人类皮肤的光学特性J Invest Dermatol 77, 13-19 (1981) 。
20. Agache, P. 皮肤结构成分: 生理学和计量学, 17-399 (Springer-Verlag, 柏林, 2014) 。
21. 梅格林斯基岛V. & Matcher, S. 皮肤反射光谱的计算机模拟。Computer Methods and Programs in Biomedicine 70, 179-186 (2003) .
22. Reuss, J. L. 反射式脉搏血氧仪的多层模型。IEEE Trans. Biom. Eng. 52, 153 - 159 (2005) 。
23. Huelsbusch, M. 基于图像的皮肤血流光电检测的函数方法。亚琛工业大学博士论文 (德文) (2008年) 。
24. Bergstrand, S., 林德伯格湖G., Ek, A. C. 的方法, 林登, M. & Lindgren, M. 使用光电体积描记术和激光多普勒技术测量不同深度的血流。皮肤15, 139-147 (2009) 。
25. 拉马特河, 雅戈迈吉湾& Talts, J. 数字脉搏容积和动脉顺应性的校准光电体积描记估计。临床生理学和功能成像27, 354-362 (2007) 。
26. 巴兰大学, 崔, W. J. & Wang, R. K. 基于oct的微血管造影在临床皮肤病学中的潜在应用。皮肤研究和技术22, 238-246 (2016) 。
27. 穆尼什河皮肌炎中甲襞毛细血管发现与疾病活动之间的关联。流变学50, 1091-1098 (2011) 。
28. 巴兰大学, 什湖, 加-地和王河K. 应用光学微血管造影技术于人类手指表皮毛细血管血流成像。J. biophotonics 8, 46-51 (2015) 。
29. Secomb, T. W., 许河, 巴西-地& Pries, A. R. 红细胞在具有内皮表面层的毛细血管中的运动: 流速的影响。Am J Physiol Heart Circ Physiol 281, 629-636 (2001) .
30. 沃尔科夫, M. V. 等人, 视频毛细血管镜检查阐明了光电体积描记波形出现的机制。科学报告7, 13298 (2017) 。
31. Mahler, F., Muheim, M. H., Intaglietta, M., Bollinger, A. & Anliker, M. 人体甲襞毛细血管的血压波动。美国生理学杂志-心脏和循环生理学236, 888-893 (1979) 。
32. 希基, M., 菲利普斯, J. P. & Kyriacou, P. A. 不同手位高度血管变化对光电容积脉搏波信号的影响。生理学测量36, 425-440 (2015) 中描述的。
33. Jacques, S. L. 和王湖, 加-地Monte Carlo Modeling of Light Transport in Tissues, 73-100 (Springer US, Boston, MA, 1995) 。
34. Wong, R., 盖耶, Weninger, W., Guimbretieau, J. C. & Wong, J. K. 皮肤的动态解剖和图案。实验皮肤病学92-98 (2015) 。
35. 盖耶, S. H. Nohammer, M. M., 廷霍夫岛E. & Weninger, W. J. 人类拇指垫的真皮动脉。Journal of Anatomy 223, 603-609 (2013) .
36. Bashkatov, A. N., Genina, E. A. & Tuchin, V. V. 皮肤、皮下和肌肉组织的光学特性: 综述。Journal of Innovative Optical Health Sciences 04, 9-38 (2011) .
37. Jacques, S. L. 生物组织的光学特性: 综述。Phys Med Biol 58, 37-61 (2013) .
38. 佐尼奥斯湾& Dimou, A. 人体在体皮肤的光散射光谱研究。Optics Express 17, 1256-1267 (2009) .
39. Shimada, M., Yamada, Y., Itoh, M. & Yatagai, T. 用多重回归分析研究人类皮肤模型中的黑色素和血液浓度: 蒙特卡罗模拟评估。Phys Med Biol 46, 2397-406 (2001) .
40. Delgado Atencio, J. A. 等人, 探针压力对人体皮肤漫反射光谱测量的影响。Optical Memory and Neural Networks 18, 6-14 (2009) .
41. 赖夫河等, 对受到不同探针压力的生物组织的反射率测量的变化的分析。Journal of Biomedical Optics 13, 010502-010502-3 (2008) 。
42. Bjorgan, A., 米兰尼奇湾& Randeberg, L. L. 实时超光谱成像应用中皮肤光学参数的估计。Journal of Biomedical Optics 19, 066003-066003 (2014) .
43. 科拉尔湖F.、佩兹, G. & Strojnik, M. 非接触式反射式光电容积描记术的最佳波长选择。在Proc. SPIE, 第8011卷, 801191-801191-7 (2011) 中。
44. 布莱克福德, E. B., Estepp, J. R. & McDuff, D. J. 应用于成像光电体积描记术的血容量脉搏的远程光谱测量。In SPIE BiOS, vol. 10501, 8 (SPIE) (2018) .
45. Aleradine, E. 等人的Next-generation acceleration and codoptimization for light transport in optical media using GPU 。Biomedical Optics Express 1, 658-675 (2010) .
46. Verma, G. 组织学基础 (新时代国际 (P) 有限公司, 出版社, 2001年) 。
47. 山口, Y. & 听力, V. J. 黑素细胞及其疾病。Cold Spring Harb Perspect Med 4, a017046 (2014) 。
48. Tuchin, V. V. 等人, 手指组织模型和血液灌注皮肤组织体模。在Proc. SPIE, 第7898卷, 78980-78980-11 (2011) 中。
49. Yudovsky, D. & Pilon, L. 从活体光谱反射测量中检索皮肤特性。J Biophotonics 4, 305-314 (2011) .
50. 施密特, J.M., Zhou, G. X., 步行者, E. C. & Wall, R. T. 光子在皮肤中扩散的多层模型。美国光学会杂志A. 7, 2141-2153 (1990) 中所述。
51. 布雷弗曼岛M. 皮肤微循环的解剖学和生理学, 第1卷, 第3-22页 (CRC出版社, 博卡拉顿, 佛罗里达, 1995) 。

52. Palmer, K. F. & Williams, D. Optical properties of water in the near infrared. *Journal of the Optical Society of America* **64**, 1107–1110 (1974).
53. Smith, R. C. & Baker, K. S. Optical properties of the clearest natural waters (200–800 nm). *Appl Opt* **20**, 177–184 (1981).
54. Salomatina, E., Jiang, B., Novak, J. & Yaroslavsky, A. N. Optical properties of normal and cancerous human skin in the visible and near-infrared spectral range. *J Biomed Opt* **11**, 064026 (2006).
55. Simpson, C. R., Kohl, M., Essenpreis, M. & Cope, M. Near-infrared optical properties of *ex vivo* human skin and subcutaneous tissues measured using the Monte Carlo inversion technique. *Phys Med Biol* **43**, 2465–2478 (1998).
56. Wim, V. *et al.* Modelling light distributions of homogeneous versus discrete absorbers in light irradiated turbid media. *Physics in Medicine and Biology* **42**, 51–65 (1997).
57. Bosschaart, N., Edelman, G. J., Aalders, M. C. G., van Leeuwen, T. G. & Faber, D. J. A literature review and novel theoretical approach on the optical properties of whole blood. *Lasers in Medical Science* **29**, 453–479 (2014).
58. Reuss, J. L. & Siker, D. The pulse in reflectance pulse oximetry: Modeling and experimental studies. *Journal of Clinical Monitoring and Computing* **18**, 289–299 (2004).
59. Graaff, R., Dassel, A. C. M., Zijlstra, W. G., Mul, F. F. M. & Aarnoudse, J. G. *How Tissue Optics Influences Reflectance Pulse Oximetry*, 117–132 (Springer US, Boston, MA, 1996).
60. Wang, L. V. & Wu, H. I. *Rayleigh Theory and Mie Theory for a Single Scatterer*, 17–35 (John Wiley & Sons, Inc., 2009).

Acknowledgements

We are thankful to Stefanos Andreou and Dr Erwin Bente (COBRA Research Institute, Eindhoven University of Technology) for allowing access to a videomicroscope. Our gratitude is extended to Dr Marius Boamfa (Multiphysics and Optics Group, Philips Corporate Technologies) for kindly borrowing light equipment, as well as to Martijn Koedam and Mark van Gastel for their efforts into GPU configuration (Electronic Systems Group, Eindhoven University of Technology). Lastly, we thank Dr Wim Verkruisse (Standartization Research, Philips Research, Eindhoven) for constructive discussions.

Author Contributions

A.M. conceived and conducted experiments, analyzed the results and drafted the manuscript. G.d.H. conceived the idea of PPG signals as a mixture of skin layers signatures and contributed to the interpretation of experimental results. All authors contributed to experimental planning and reviewed the manuscript.

Additional Information

Supplementary information accompanies this paper at <https://doi.org/10.1038/s41598-018-26068-2>.

Competing Interests: The authors declare no competing interests.

Publisher's note: Springer Nature remains neutral with regard to jurisdictional claims in published maps and institutional affiliations.



Open Access This article is licensed under a Creative Commons Attribution 4.0 International License, which permits use, sharing, adaptation, distribution and reproduction in any medium or format, as long as you give appropriate credit to the original author(s) and the source, provide a link to the Creative Commons license, and indicate if changes were made. The images or other third party material in this article are included in the article's Creative Commons license, unless indicated otherwise in a credit line to the material. If material is not included in the article's Creative Commons license and your intended use is not permitted by statutory regulation or exceeds the permitted use, you will need to obtain permission directly from the copyright holder. To view a copy of this license, visit <http://creativecommons.org/licenses/by/4.0/>.

© The Author(s) 2018

52. 帕默, K. F. & 威廉姆斯, D. 水在近红外波段的光学性质。Journal of the Optical Society of America 64, 1107-1110 (1974) .
53. 史密斯河C. & Baker, K. S. 最清澈的天然沃茨的光学特性 (200-800 nm) 。Appl Opt 20, 177-184 (1981) .
54. Salomatina, E., Jiang, B., Novak, J. & Yaroslavsky, A. N. 正常和癌变人类皮肤在可见光和近红外光谱范围内的光学特性。J Biomed Opt 11, 064026 (2006) .
55. 辛普森角R., Kohl, M., Essenpreis, M. & 科普, M. 使用蒙特卡罗反演技术测量离体人体皮肤和皮下组织的近红外光学特性。Phys Med Biol 43, 2465-2478 (1998) .
56. Wim, V. 等人, 光照射混浊介质中均匀吸收体与离散吸收体的光分布建模。Physics in Medicine and Biology 42, 51-65 (1997) .
57. Bosschaart, N., Edelman, G. J., 奥尔德斯, M. C. G., 货车Leeuwen, T. G. & Faber, D. J. 关于全血光学性质的文献综述和新的理论方法。Lasers in Medical Science 29, 453-479 (2014) .
58. Reuss, J. L. & Siker, D. 反射式脉搏血氧仪中的脉搏: 建模和实验研究。Journal of Clinical Monitoring and Computing 18, 289-299 (2004) .
59. 格拉夫河, Dassel, A. C. M., Zijlstra, W. G., 穆尔, F. F. M. & Aarnoudse, J. G. 组织光学如何影响反射脉搏血氧仪, 117-132 (Springer US, Boston, MA, 1996) .
60. 王湖, 加地V. & Wu, H. I. Rayleigh Theory and Mie Theory for a Single Scatterer, 17-35 (John Wiley & Sons, Inc., 2009年) .

确认

感谢Stefanos Andreou和Erwin Bente博士（埃因霍温理工大学眼镜蛇研究所）允许使用视频显微镜。我们感谢Marius Boamfa博士（多物理和光学组，飞利浦公司技术），感谢他们借用照明设备，感谢Martijn Koedam和Mark货车Gastel为GPU配置所做的努力（电子系统组，埃因霍温理工大学）。最后，我们感谢Wim Verkruisse博士（标准化研究，飞利浦研究，埃因霍温）的建设性讨论。

作者贡献

上午构思并进行实验，分析结果并起草手稿。G.d.H.设想PPG信号作为皮肤层签名的混合物的想法，并有助于解释实验结果。所有作者都参与了实验计划并审查了手稿。

附加信息

本文的补充信息见<https://doi.org/10.1038/s41598-018-26068-2>。

竞争利益：作者声明没有竞争利益。

出版商说明：施普林格·自然在出版地图和机构附属机构的管辖权主张方面保持中立。



根据知识共享署名4.0国际许可协议进行许可，该协议允许以任何媒介或格式使用、共享、改编、分发和复制，只要您给予适当的署名给原作者和来源，提供知识共享许可协议的链接，并注明是否进行了更改。本文中的图像或其他第三方材料包含在文章的知识共享许可证中，除非在材料的信用额度中另有说明。如果材料未包含在文章的知识共享许可中，并且您的预期用途不受法律法规的允许或超出了允许的用途，则您需要直接从版权保持器获得许可。要查看本许可证的副本，请访问<http://creativecommons.org/licenses/by/4.0/>。

©作者 (S) 2018